12-3-2021

Implications from Uranium-Series Disequilibria in a Bi-lithologic Melt with Varying Lithospheric Caps

Juliet Messer
University of Nebraska-Lincoln, jmesser2@huskers.unl.edu

IMPLICATIONS FROM URANIUM-SERIES DISEQUILIBRIA IN A BI-LITHOLOGIC MELT WITH VARYING LITHOSPHERIC CAPS

by

Juliet F. D. Messer

A THESIS

Presented to the Faculty of

The Graduate College at the University of Nebraska

In Partial Fulfillment of Requirements

For the Degree of Master of Sciences

Major: Earth and Atmospheric Sciences

Under the Supervision of Professor Lynne J. Elkins

Lincoln, Nebraska

November, 2021

IMPLICATIONS FROM URANIUM-SERIES DISEQUILIBRIA IN A BI-LITHOLOGIC MELT WITH VARYING LITHOSPHERIC CAPS

Juliet F. D. Messer, M.S.

University of Nebraska, 2021

Advisor: Lynne J. Elkins

Both spreading rates and local magma supply to mid-ocean ridges affect crustal construction styles and ridge morphology, alternately leading to either asymmetrical (detachment faulting) or symmetrical faulting styles. Uranium-series isotopic disequilibria in mid-ocean ridge basalts (MORB) may provide insight into how melt supply variations relate to ridges' accretion styles, a processes that are not well understood. I use Reactive Porous Flow (RPF) equilibrium and disequilibrium modeling to simulate U-series disequilibria at mid-ocean ridge (MOR) generated by melt supply variations at both asymmetrical and symmetrical ridge segments.

Guided by my modeling, I predict that enhanced melt contributions from enriched pyroxenitic mantle produce elevated ($^{230}Th/^{238}U$) in young basalts due to the higher garnet modes in pyroxenites throughout the melting regime. If symmetrical segments of the Kane-Atlantis Supersegment overlie more pyroxenite-rich mantle zones, as postulated here, I would expect measurably higher ($^{230}Th/^{238}U$) in basalts from those areas. Lack of such a systematic signature along symmetrical segments would alternatively suggest that

crustal magma pooling patterns dominantly control melt supply variations along slow-spreading ridges without an underlying mantle driving force. The ($^{226}Ra/^{230}Th$) and ($^{231}Pa/^{235}U$) ratios of the RPF equilibrium and disequilibrium models generate results that do not fully explain the global MORB data using a single melting lithology. The model results suggest that mixing melts from multiple mantle sources may be necessary to produce the full global data set. Comparing these preliminary results to traditional dynamic melting models and radiogenic isotopes may provide additional insight into how the mantle melting process truly affects both U-series isotopes and ridge symmetry.

Acknowledgements

I want to start by thanking my advisor, Dr. Lynne J. Elkins, from the Department of Earth and Atmospheric Sciences at the University of Nebraska-Lincoln. Dr. Elkins has helped me in many ways by providing me with fantastic, valuable feedback and support when performing lab procedures and writing. I want to thank her for sharing her 2019 data set and taking the time to explain and guide me on how to use the modeling software.

Many thanks to the National Science Foundation for funding this project (grant number: OCE-MGG-1658011) and the Department of Earth and Atmospheric Sciences for offering me the Research Assistantship, use of the U.N.I.T.E. Geochemistry Lab, and a Teaching Assistantship. This thesis would not have been possible without their generous funding.

I want to thank my committee members, Dr. Caroline M. Burberry and Dr. Richard M. Kettler, for their help, encouragement, and taking the time to teach me about various geologic topics.

I would also like to thank Dr. Kenneth W. W. Sims and Lisa B. Kant of the University of Wyoming for running my U, Th, and Ra samples on their ICP-MS and giving valuable feedback. I also want to thank them for being flexible while making arrangements for my sample analysis during the pandemic.

Lastly, I would like to thank my family, friends, and partner, Noah, for the support, love, and reminders to take a break. I would also like to thank my lab mates Nicholas Richard and Kirby Hobbs for making me laugh, helping to answer my questions, and providing an environment where I could learn and ask questions without judgment. Finally, I would like to thank the essential workers who kept the university open and running. Without everyone's encouragement and support, my thesis would not have gotten finished.

Juliet Florence DeMedici Messer

Table of Contents

1. Introduction**.....1**

2. Background**.....7**

2.1. Mid-ocean ridge systematics.....7

2.1.1. Mid-ocean ridge settings.....7

2.1.2. Tectonic controls on mid-ocean ridge construction.....8

2.1.3. Underlying mantle characteristics and dynamics.....13

2.1.4. Lithologic heterogeneity in the mantle.....15

2.2. Uranium-series in MORB.....16

2.2.1. Uranium-series isotopes.....16

2.2.2. Uranium-series: Effects of mantle heterogeneity.....19

2.3. Melting models.....21

2.3.1. Dynamic Melting.....22

2.3.2. Reactive porous flow melting.....25

2.4. Geologic Setting.....29

2.4.1. The Kane Atlantis Supersegment.....29

3. Methods**.....32**

3.1. Model rationale.....32

3.1.1. Model background and software.....32

3.1.2. Modeling variables.....36

4. Results**.....40**

4.1. RPF equilibrium and disequilibrium transport results: (^{230}Th/^{238}U).....48

4.2. RPF equilibrium transport results: (^{226}Ra/^{230}Th) and (^{231}Pa/^{235}U).....49

4.3. RPF disequilibrium transport results: (^{226}Ra/^{230}Th) and (^{231}Pa/^{235}U).....50

***5. Discussion*.....52**

5.1. Lithologic transport effects on U-series disequilibria.....52

5.1.1. Lithospheric thickness effects.....52

5.1.2. Transport mechanism and mixing effect.....55

5.2. Implications of results from Melting Models.....58

5.3. Ridge symmetry and supporting geochemical data.....65

***6. Conclusion*.....67**

***7. References*.....69**

***8. Appendix A*.....85**

List of Tables

1. List of variables used in model calculations.....39
2. Summary of modeling results for equilibrium and disequilibrium before and after lithospheric decay.....51

3. Supplementary table of solid/liquid partition coefficients.....85-86

List of Figures

1. Global bathymetric and topographic map of the Kane-Atlantis Supersegment.....5

2. Asymmetrical versus Symmetrical Accretion.....8

3. Bathymetric map of the OCC south of the Kane Fracture Zone.....12

4. Steady-state passive upwelling of and melting regime model.....14

5. The decay chain of the ^{238}U-series & ^{235}U-series.....17-18

6. Dynamic melting model with two-lithology melting regime.....23

7. Dynamic melting versus RPF melting model.....26

8. RPF melting model with bilithologic melting regime.....27

9. Bathymetric map of the Kane-Atlantis Supersegment.....30

10. Gridded results for RPF equilibrium transport melting at 10 kbar.....41

11. Gridded results for RPF equilibrium transport melting 10 kbar post-decay.....42

12. Gridded results for RPF equilibrium transport melting at 15 kbar.....43

13. Gridded results for RPF equilibrium transport melting 15 kbar post-decay.....44

14. Gridded results for RPF disequilibrium transport melting at 10 kbar.....45

15. Gridded results for RPF disequilibrium transport melting 10 kbar post-decay.....46

16. Gridded results for RPF disequilibrium transport melting at 15 kbar.....47

17. Gridded results for RPF disequilibrium transport melting 15 kbar post-decay.....48

18. Gridded results for dynamic melting at 0.5 GPa.....61

19. Gridded results for RPF disequilibrium transport melting at 5 kbar.....62

1. Introduction

Mid-ocean ridge (MOR) systems are found throughout the world in Earth's oceans and are responsible for constructing new ocean crust (Smith et al., 2006). As the plates diverge at the ridge, passive upwelling decompresses mantle rocks, resulting in partial melts, which rise due to buoyancy differences between the magma and mantle rocks (Scott & Stevenson, 1989; Smith & Cann, 1993). The crust at mid-ocean ridges is primarily composed of gabbros and mid-ocean ridge basalts (MORB) (Klein & Langmuir, 1987; Olive & Escartín, 2016). Mid-ocean ridge basalts are formed when the mantle decompresses and the magma rises and erupts on the seafloor (Buck et al., 2005; Colman et al., 2012; Klein & Langmuir, 1987; Smith & Cann, 1993). Some fundamental questions remain regarding oceanic crustal formation due to emplacement of the resulting magma: how is gabbroic magma emplaced under the ridge, and how does that emplacement affect axial faulting at slow-spreading mid-ocean ridges? What controls the supply or volume of melt, contributing to crustal growth?

The oceanic crustal construction system at MORs has been studied for decades, yet there is still disagreement regarding the details of magma transport and emplacement, oceanic crustal construction, and ridge symmetry. In the last half-century, several studies have published MOR observations and data and explored oceanic crustal construction mechanisms and their causes (e.g., Bourdon et al., 1996; Dick et al., 2008; Elkins et al., 2014, 2016, 2019; Hirschmann & Stolper, 1996; Hofmann, 1997, 2003; Klein & Langmuir, 1987, 1989; Kogiso et al., 2004; Lee & Chin, 2014; McKenzie et al., 2004;

Petermann & Hirschmann, 2003; Prytulak & Elliott, 2009; Rudge et al., 2013; Standish et al., 2008; Wilson et al., 2013; White and Klein, 2013). Construction at mid-ocean ridges happens through a combination of tectonic processes and magmatic emplacement (Blackman et al., 1998, 2009; Colman et al., 2012; Scott & Stevenson, 1989; Smith & Cann, 1993). Along with variations in the relative importance of tectonic extension and magmatic emplacement, magma supply variations along a ridge axis may affect ridge symmetry, leading to symmetrical and asymmetrical crustal accretion styles that affect seafloor morphology (Escartín et al., 2008; Murton & Rona, 2015; Olive & Escartín, 2016; Scott & Stevenson, 1989; Smith et al., 2008, 2012; Lyu, 2019).

Many prior studies have considered crustal accretion and MORB genesis to be dependent on variations in mantle temperature, melt transport differences, lithospheric thickness, or mantle source heterogeneity. Some have suggested that mantle temperature beneath the mid-ocean ridge is the main factor driving the extent of mantle melting and resulting oceanic crustal thickness (e.g., Asimow et al., 2004; Guo et al., 2021; Klein & Langmuir, 1987). Other studies suggest that lithospheric thickness may play a role in detachment faulting and ridge symmetry by shortening the top of the melting column (e.g., Escartín et al., 2008; Humphris et al., 2015; Naliboff et al., 2012; Peirce et al., 2019). Still, other studies have considered mantle source heterogeneity to be the main driving factor that determines ridge construction mechanisms and seafloor morphology both locally and globally (Elkins et al., 2011, 2016a, 2019; Gale et al., 2013; Lissenberg & Dick, 2008; Lyu, 2019; Murton & Rona, 2015; Niu et al., 2001; Waters et al., 2011). Mantle heterogenies can be measured using major and trace elements and Uranium-series isotopes (e.g. Gale et al., 2013; Elkins et al., 2016a, 2019; Lyu, 2019).

Uranium-series isotopes are valuable geochemical tools for evaluating the role of mantle source heterogeneities during melting as their half-lives are comparable to the variable melting rates of common mantle lithologies (Bourdon et al., 2003; McKenzie, 1985; Russo et al., 2009; Spiegelman & Elliott, 1993; Standish & Sims, 2010; Stracke et al., 2003). U-series are also a useful tool for tracking the mechanisms of magma transport in the melt zone and potentially through the lithosphere using melting models.

McKenzie (1985) developed the dynamic melting model to track U-series disequilibria in instantaneously extracted, "near fractional" partial melts. An alternative model for melt generation and migration is reactive porous flow (RPF), which tracks the fractionation and ingrowth of U-series isotopes during partial melting and magma migration through an effectively chromatographic melting column (Spiegelman & Elliott, 1993). Both RPF and dynamic melting models can predict U-series isotope concentrations and activities, which can be compared to global MORB data to attempt to explain global magma origins and the nature of the melting process (Elkins et al., 2016, 2019; Lambart et al., 2016; McKenzie, 1985; Hirschmann and Stolper, 1996; Pertermann and Hirschmann et al., 2003; Russo et al., 2009; Spiegelman & Elliott, 1993). The approach for this study compares RPF melting model results to MORB data. The model results may provide insight into melt supply and transport affects on the measurable U-series isotopes and can then be compared to major and trace elements.

While the nature of the melting process (e.g., equilibrium vs. chemical disequilibrium between the migrating solid and liquid) has a significant effect on magma composition in these models, differences in U-series disequilibria may also be affected by the lithologic composition of the mantle source; different mantle rocks (e.g., peridotite

versus pyroxenite) should melt at dramatically different rates and may contain different minerals (Lambart et al., 2016; Langmuir et al., 1992; Pertermann & Hirschmann, 2002; Stracke & Bourdon, 2009). This study will explore the effects of lithospheric thickness and mantle source heterogeneities under slow-spreading ridge conditions and will be related to Lyu's (2019) major and trace element data from the Kane-Atlantis Supersegment. One of the main goals of this study is to relate U-series modeling results and major and trace elements to determine melt supply variation effects on crustal accretion styles.

The Kane Atlantis Supersegment (24° N-31° N) of the Mid-Atlantic Ridge (MAR) is a slow-spreading ridge that provides a useful area to explore varying crustal construction styles (Figure 1, Murton & Rona, 2015). Slow spreading mid-ocean ridges may account for ~80% of the global mid-ocean ridge system (Murton and Rona, 2015).

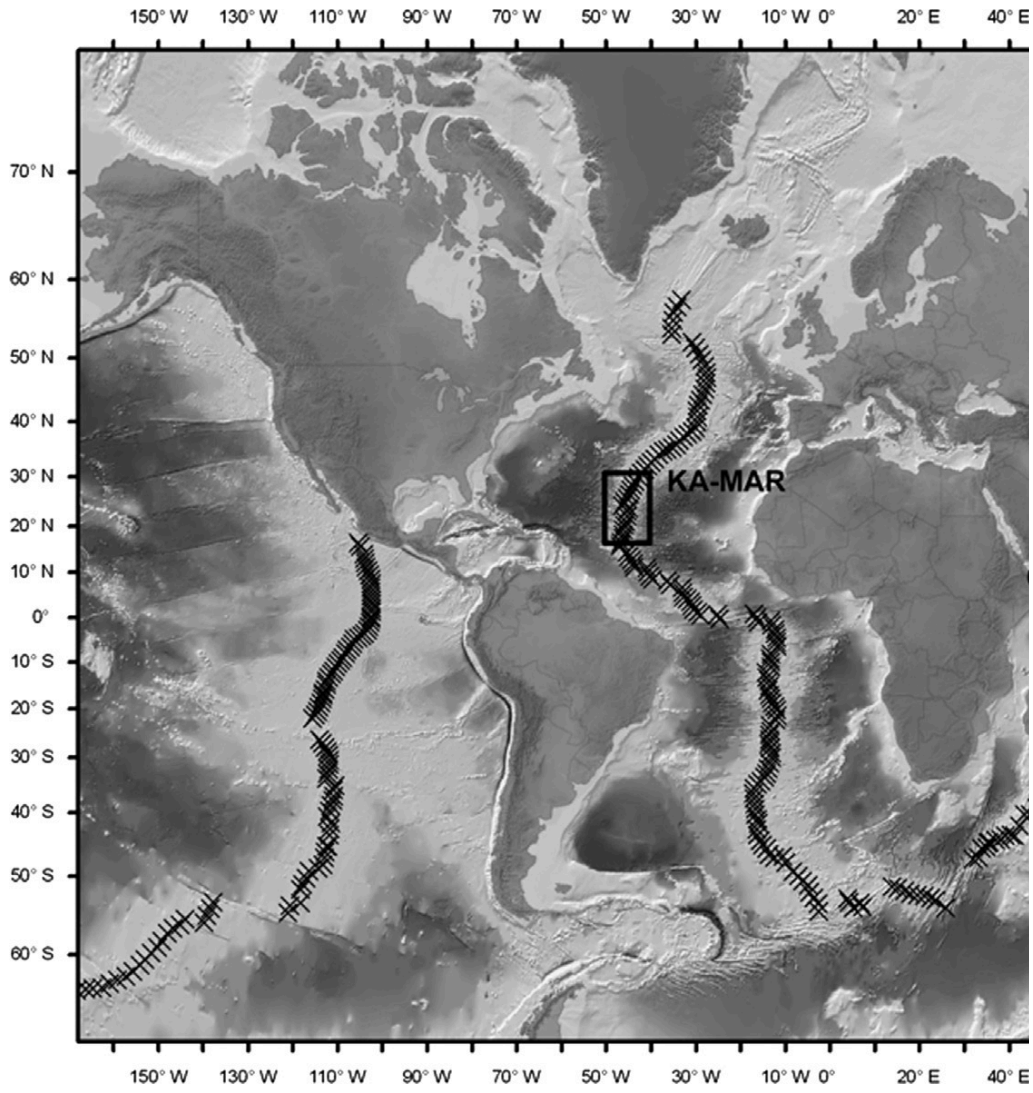

Figure 1. Global bathymetry and topographic map showing the Kane- Atlantis Supersegment of the Mid-Atlantic Ridge (KA-MAR). Crosses show locations of the centers of second-order ridge segments for the major mid-ocean ridges (modified from Murton & Rona, 2015).

Slow-spreading ridges like the Kane-Atlantis Supersegment exhibit both asymmetrically (detachment fault-bearing) and symmetrically accreted second-order ridge segments (Murton & Rona, 2015; Smith et al., 2012; Standish & Sims, 2010; Yu et al., 201). Studies suggest that magma supply and composition may drive faulting style and crustal accretion modes, affecting seafloor morphology and producing geochemical

differences in MORB composition (Escartín et al., 2008; Lyu, 2019; Murton & Rona, 2015; Smith et al., 2008). Differences in geochemical signatures in basalts from both symmetrically and asymmetrically accreted ridge segments may record the underlying melt generation and transport processes. This is important because differences in geochemical signatures (e.g., U-series isotopes and major and trace elements) may contribute to our understanding of the relationships between accretion style and magma supply variations at slow-spreading mid-ocean ridges.

This study examines the role of mantle heterogeneities on U-series disequilibria in MORB under slow-spreading ridge conditions, using both equilibrium and disequilibrium RPF melting models. I also test for the additional role of varying lithospheric thicknesses of 10 kbar and 15 kbar to represent thicker lithosphere under slow- and ultra-slow spreading ridge conditions (Naliboff et al., 2012; Peirce et al., 2019). Here I compare model outcomes to the global MORB data set to determine: (1) whether varying lithospheric cap thicknesses at 15 kbar (46 km), and 10 kbar (30 km) cause measurable differences in U-series disequilibria; (2) whether the U-series disequilibria predicted by the RPF models in partial melts are comparable to the global MORB data, for a range of lithologic types; (3) how future U-series results, in combination with major and trace element measurements in MORB, could be used to determine the extent to which heterogeneities affect crustal accretion modes and ridge symmetry at the Kane-Atlantis Supersegment; and (4) whether RPF models better reproduce the global MORB data than traditional dynamic melting models and which model might be better applied to future U-series analysis of the Kane-Atlantis Supersegment .

2. Background

2.1 Mid-ocean ridge systematics

2.1.1 Mid-ocean ridge settings

The global system of MOR is responsible for the creation of new oceanic crust (Macdonald et al., 1988; Murton & Rona, 2015; Olive & Escartín, 2016; Smith & Cann, 1993; Smith et al., 2006, 2012). Spreading rates range from fast (>10 cm/yr) through intermediate (5.5-10 cm/yr) and slow (5.5-2.0 cm/yr), to ultraslow (< 2.0 cm/yr). The MOR system accounts for ~70% of global magmatism and generates two-thirds of Earth's new crust (Gale et al., 2013; Smith & Cann, 1993; Smith et al., 2012; Standish & Sims, 2010). Average crustal thickness of mid-ocean ridges is relatively uniform, between 5-7 kilometers thick, with the crust being 0 kilometers thick at the ridge center of fast-spreading ridges (Naliboff et al., 2012). Lithospheric thickness varies from 0 kilometers at the ridge center of fast spreading ridges to 100 kilometers in older oceanic plates (Naliboff et al., 2012; Pierce et al., 2019).

Slow-spreading ridges constitute ~80% of the total global MOR length and it is critically important to gain a greater knowledge of the driving forces along slow-spreading centers to better understanding the global tectonic system (Murton & Rona, 2015). Slow-spreading ridges are also unique in hosting both symmetrical (i.e., typical normal faulting) and asymmetrical (i.e., detachment faulting) accretion styles in roughly equal proportions (Murton & Rona, 2015). Intermediate- and fast-spreading ridges are dominated by symmetrical accretion (Olive & Escartín, 2016; Smith & Cann, 1993; Smith et al., 2006, 2012). The ultraslow-spreading ridges are characterized by

amagmatic, fault-dominated accretion, and detachment faults (Standish & Sims, 2010). Both crustal accretion styles can be seen in Figure 2 (Escartín et al., 2008).

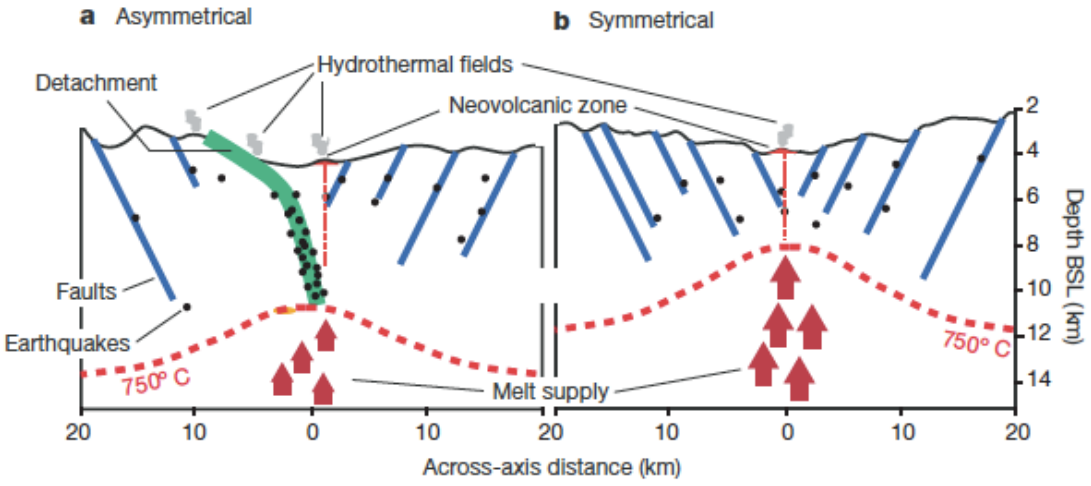

Figure 2. Asymmetrical (**a**.) and symmetrical (**b**.) accretion (Escartín et al., 2008). The dashed red line indicates the top of the melting regime with melting temperatures of 750°C. Red arrows indicate ascending magma. **a.** The green line is the detachment fault that truncates the top of the melting column, resulting in low extents of mean melting and a thick lithosphere. **b.** Symmetrical accretion without melting column truncation resulting in thinner lithosphere.

2.1.2 Tectonic controls on mid-ocean ridge construction

The purpose of this study is to investigate the driving factors of magma supply and its effects on crustal construction styles at slow-spreading ridges. Understanding the crustal construction styles is necessary to understand magma emplacement at a MOR setting and its tectonic controls.

Passive upwelling and partial melting of the mantle occurs when the two overlying plates diverge, causing the solid asthenosphere to rise in response (Blackman et al., 1998; Scott & Stevenson, 1989; Smith & Cann, 1993; White & Klein, 2013). While

passive upwelling happens in response to tectonic extension, mantle asthenosphere can also actively upwell in hotspot regions, which may be situated near passive upwelling cells, creating a combination of tectonic and active (i.e., mantle-plume driven) mantle decompression followed by magmatic emplacement (Blackman et al., 1998, 2009; Colman et al., 2012; Scott & Stevenson, 1989; Smith & Cann, 1993).

Along a ridge axis, typically broken into discrete segments, magma is supplied in greater volumes to the segment centers than to the segment ends, broadly resulting in a thicker oceanic crust at the center (Coleman et al., 2012; Smith & Cann, 1993). Perpendicularly across each segment, the spreading axis is narrow, with most magmatic activity happening in a narrow neovolcanic zone, even at ultraslow-spreading rates where magma supply is especially low (Standish & Sims, 2010). The higher magmatic activity at the center of the ridge suggests that melt either: 1. accumulates and pools beneath the center of each segment, migrates, and then moves laterally along the axis for a limited distance; or 2. disperses vertically from the underlying mantle melt zone along the entire segment without pooling, but with more significant upwelling in the mantle beneath the segment's center (Coleman et al., 2012; Smith & Cann, 1993; Smith et al., 2012). Uranium-series eruption ages of volcanic rocks at ultra-slow spreading ocean ridges have further identified young basaltic rocks throughout the rift valley; this indicates that at least in less magmatically-driven settings, volcanic activity is not confined to the spreading axis, and magma can likely travel to the surface along faults (Standish & Sims, 2010).

Tectonic extension combined with magmatic activity contributes to the crustal accretion style (i.e., symmetrical versus asymmetrical faulting) and may be influenced by

the supply and emplacement depths of magma derived from the underlying mantle, affecting magma supply leading to symmetrical and asymmetrical crustal accretion (Escartín et al., 2008; Murton & Rona, 2015; Olive & Escartín, 2016; Scott & Stevenson, 1989; Smith et al., 2008, 2012). As noted above, symmetrical accretion is typically dominant along intermediate- and fast-spreading ridges and is associated with robust volcanic activity (Standish & Sims, 2010). Symmetrical accretion and the associated, underlying high magma flux likely bury the symmetrical, high-angle normal faults that frame the axial valley, creating a smooth and inflated morphology (Escartín et al., 2008; Murton & Rona, 2015; Standish & Sims, 2010). MacLeod et al. (2009) proposed that magma supply to the spreading center exerts a primary control over the presence or absence of detachment faulting (i.e., asymmetrical or symmetrical accretion), suggesting that magma supply is a key driver of ridge symmetry.

Detachment faults are long-lived (some recording active slip duration for as long as 1-2 Ma on a single fault surface; Sloan & Patriat, 2004), and a single active detachment fault can extend several kilometers away from the ridge axis (Smith et al., 2006, 2012). Detachments are associated with high seismicity caused by tectonic strain and increased oceanic lithospheric thickness from the decreased magmatic activity; a detachment ultimately terminates when cut by a newer fault as the plates diverge (Cann et al., 1997; Escartín et al., 2008; Humphris et al., 2015a; MacLeod et al., 2009; Murton & Rona, 2015; Smith et al., 2006, 2012; Tucholke & Lin, 1998). The thickening of the lithosphere due to detachment faults also shortens the underlying mantle melting column by truncating the decompressing column at depth (Escartín et al., 2008). Detachment

faults along asymmetric segments are also underlain by deep, crystal mush zones where extensive melt-rock interactions likely occur (Lissenberg & Dick, 2008).

Across an asymmetrical segment, the thicker lithosphere associated with active detachment faults contributes to slower migration from the ridge axis when compared to the symmetrical faults observed along fast-spreading ridges; this causes an accumulation of large offsets and mature detachment faults in the seafloor produced by slow-spreading, asymmetrical ridge segments (Buck et al., 2005; Olive & Escartín, 2016; Macleod et al., 2009; Tucholke et al., 2008).

Long-lived detachment faults are also associated with oceanic core complexes (OCCs), particularly at slow and ultra-slow spreading MORs, and at inside corner highs along major transform offsets; OCCs likewise affect seafloor morphology as well as hydrothermal activity (Humphris et al., 2015b; Smith et al., 2008, 2012). Along major, well-developed detachment faults, OCCs exhume and expose lower crustal and upper mantle rocks that are then preserved in the oceanic crust after fault termination (Smith et al., 2012). Exhumation of OCCs occurs by movement along the largest, low angle detachment faults and results in off-axis, corrugated features on the seafloor known as "megamullions" (e.g., the Kane Megamullion or OCC, just south of the Kane Fracture Zone, Figure 3) (Blackman et al., 1998; Cann et al., 1997; MacLeod et al., 2009; Murton & Rona, 2015; Smith et al., 2006, 2012; Tucholke et al.,1998).

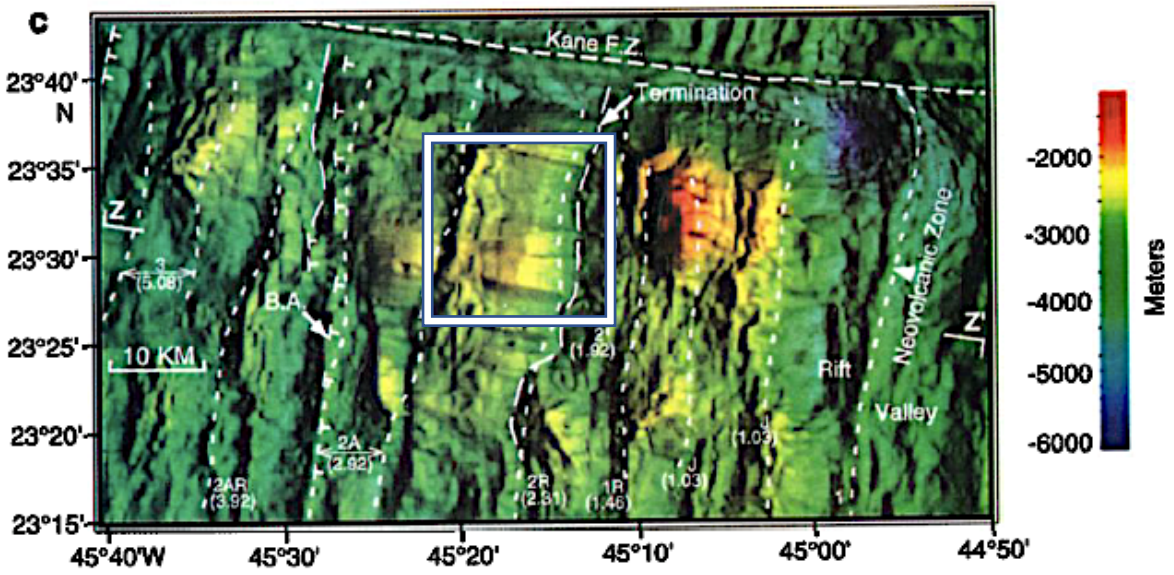

Figure 3. Bathymetric map showing the oceanic core complex (white box) south of the Kane Fracture Zone, after Tucholke et al. (1998).

The Kane OCC is located on the inside corner of the Kane Fracture Zone, and the adjacent axis has a half-spreading rate of 1.44 cm/yr (Dick et al., 2008; Zhiteng et al., 2013). Due to its proximity to the slow-spreading Kane Atlantis (KA) Supersegment, the Kane OCC is locally useful for studying detachment faults, symmetry, and magma supply variations (Murton & Rona, 2015; Humphris et al., 2015b; Tucholke et al., 1998). The Kane OCC consists of exposed gabbros and serpentinized peridotite near the exhumed footwall (e.g., Dick et al., 2008; Tucholke et al., 1998; Xu et al., 2009). The KA Supersegment also hosts many other detachment-faulted segments making it an excellent area to investigate changes in magma supply and fertility (Murton & Rona, 2015; Humphris et al., 2015b; Tucholke et al., 1998).

2.1.3 Underlying mantle characteristics and dynamics

A better understanding of magma supply variation origins, which may influence crustal accretion style, requires further exploration of mantle characteristics and dynamics under slow-spreading ridges such as the Kane-Atlantis Supersegment.

Mid-ocean ridge construction is a product of ascension and decompression of largely lherzolitic (a peridotitic rock) mantle beneath the ridge axis (Elkins et al., 2011; Klein & Langmuir, 1987; Lambart et al., 2009, and references therein). The axial ridge seafloor depth, a proxy for crustal thickness, reflects underlying regional variations in mantle temperature that drive the overall extent of mantle melting and thus the total magma flux (Bourdon et al., 1996 and references therein; Klein & Langmuir, 1987). The equivalent temperature of a mantle rock brought to the surface without melting is the potential temperature (White & Klein, 2014).

Mantle temperature plays a crucial role in this system by controlling the initial melting pressure in a passive upwelling mantle regime, as shown in Figure 4. Figure 4a shows a relatively high mantle potential temperature with a deep solidus and long melt interval, resulting in a thick overlying oceanic crust layer and large degrees of partial melting (Bourdon et al., 1996 and references therein; Elkins et al., 2011; Klein & Langmuir, 1987; White & Klein, 2014). Figure 4b shows a cooler mantle scenario (i.e., lower potential temperature) and a shorter melt column that produces thinner oceanic crust and smaller degrees of partial melting (Bourdon et al., 1996 and references therein; Elkins et al., 2011; Klein & Langmuir, 1987; Langmuir et al., 1992; White & Klein,

2014).

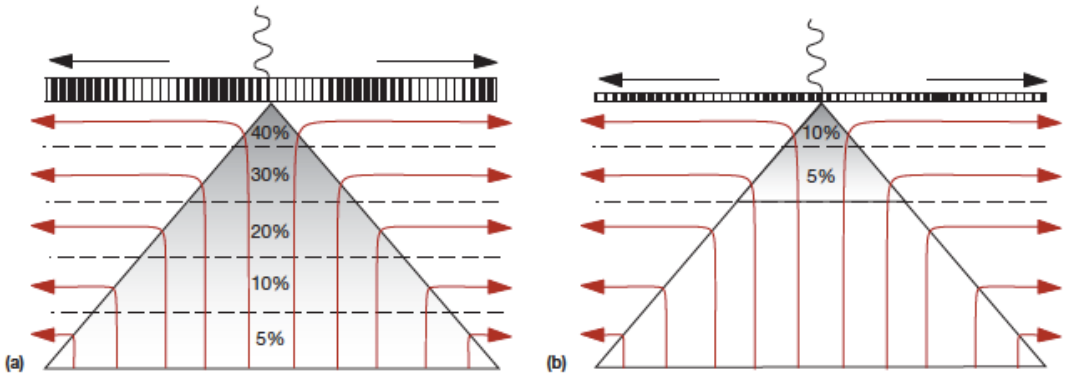

Figure 4. Steady-state passive upwelling of and melting regime model beneath mid-ocean ridges after White and Klein (2014). Red curved lines with arrows indicate solid mantle convection paths through the melting regime; dashed lines indicate the extent of melting for a simple constant melting rate. **a)** A hotter mantle intersection at deeper solidus depth, causing a larger mean and maximum extent of melting. **b)** A cooler mantle intersection at a shallower solidus depth causes a smaller mean and maximum extent of melting.

Mantle potential temperatures under mid-ocean ridges likely vary between 1300-1450 ºC (Asimow et al., 2001; Grose & Afonso, 2013; Herzberg, 2004; Langmuir et al., 1992; McKenzie & Bickle, 1988). As explained above, the initial depth of melting (i.e., solidus depth) of a peridotitic mantle depends on the source mantle's potential temperature (Klein & Langmuir, 1987; White & Klein, 2014). The solidus depth is also affected by the presence of lithologic heterogeneities, such as eclogite or pyroxenite rich veins, which in many cases are expected to begin melting at higher pressures than peridotite rocks (Bourdon et al., 1996 and references therein; Elkins et al., 2019; Lambart et al., 2016; Lambart, 2017; Lundstrom et al., 1998 a,b; Phipps Morgan, 2001).

2.1.4 Lithologic heterogeneity in the mantle

Hirschman & Stolper (1996) proposed that chemical heterogeneity in the mantle may be derived from the melting of pyroxene-rich mafic lithologies (i.e., pyroxenites) and recycled oceanic crust. Many subsequent studies support their conclusions based on measurements of major and trace elements and radiogenic isotopes in oceanic basalts (e.g., Elkins et al., 2016b, 2019; Kogiso et al., 2004; Lambart et al., 2009, 2013, 2016). However, some geochemical studies have used major and trace elements and radiogenic isotopes to suggest the presence of metasomatized peridotites rather than pyroxenite lithologies in the mantle source for some hotspots such as the Azores (e.g., Prytulak & Elliott, 2009).

According to Lambart et al. (2016), pyroxenites are a broad class of rocks that have mafic to ultramafic compositions (Kogiso et al., 2004; Lambart et al., 2013), are pyroxene abundant, and have less than 40% olivine. Garnet pyroxenites provide a possible explanation for melt generation beneath MOR, where the basalt compositions indicate the presence of residual garnet during melting (e.g., Lambart et al., 2016). Melting of mantle garnet pyroxenites could likewise potentially explain differences in crustal construction styles at mid-ocean ridges, as they melt more productively than peridotites (Lambart et al., 2016; Lambart, 2017; Elkins et al., 2019).

For this study, I concentrate on U-series isotopes which can help fingerprint the source heterogeneities present in the melting mantle. Major and trace elements can help identify the melting process and source composition in conjunction with U-series isotopes. Major element analysis (i.e., Na, Ca, Mg, Al, Fe, Ti) can suggest heterogeneities through distinct enrichment and depletion patterns (Klein & Langmuir, 1987). Trace

element signatures can provide information about source composition and melting processes in distinct, long-lived mantle reservoirs, which record trace element depletion or enrichment integrated over long periods of time (Herzberg, 2004; Hofmann, 2003; Niu et al., 2001; Klein & Langmuir, 1987; Phipps Morgan, 2001; Rudge et al., 2013; Salters & Stracke, 2004; Stracke & Bourdon, 2009).

Notably, pyroxenites exhibit different melt partitioning behavior than peridotites for certain elements (Langmuir et al., 1992; Pertermann & Hirschmann, 2002; Stracke & Bourdon, 2009). For example, strontium (Sr) isotopes are more incompatible in peridotites than in pyroxenites and can be potentially useful in determining mantle source heterogeneity (Guo et al., 2021; Niu et al., 2001; Salters & Stracke, 2004; Stracke & Bourdon, 2009). Mid-ocean ridge basalts are typically "normal-type" (N-MORB) or, less often, "enriched-type" (E-MORB), which are relatively enriched in trace elements (Hofmann, 2003; Salters & Stracke, 2004). For example, Lyu's (2019) preliminary major and trace elements results from the slow-spreading Kane-Atlantis Supersegment indicate that pyroxenite partial melts may be contributing more melt supply at symmetrical segments. Using major and trace elements in basalts in combination with U-series isotopes makes it possible to evaluate whether pyroxenites might influence melt supply at symmetrical and asymmetrical segments of the Kane-Atlantis Supersegment.

2.2 Uranium-series disequilibria in MORB

2.2.1 Uranium-series isotopes

To further investigate the origins of mid-Atlantic MORB and explore whether and how their petrogenesis is related to drivers of magma supply and crustal construction, I

aim to use computational modeling to predict U-series isotopes compositions in a bilithologic melting regime. Future U-series results from Kane-Atlantis Supersegment samples may be compared to modeling results to evaluate if models are correctly predicting melt supply variations. Naturally occurring uranium isotopes are radioactive on geologic timescales, and their decay produces a complex, step-wise decay chain of sequential radioactive nuclides (Fig. 3) (McKenzie, 1985; Spiegelman & Elliott, 1993).

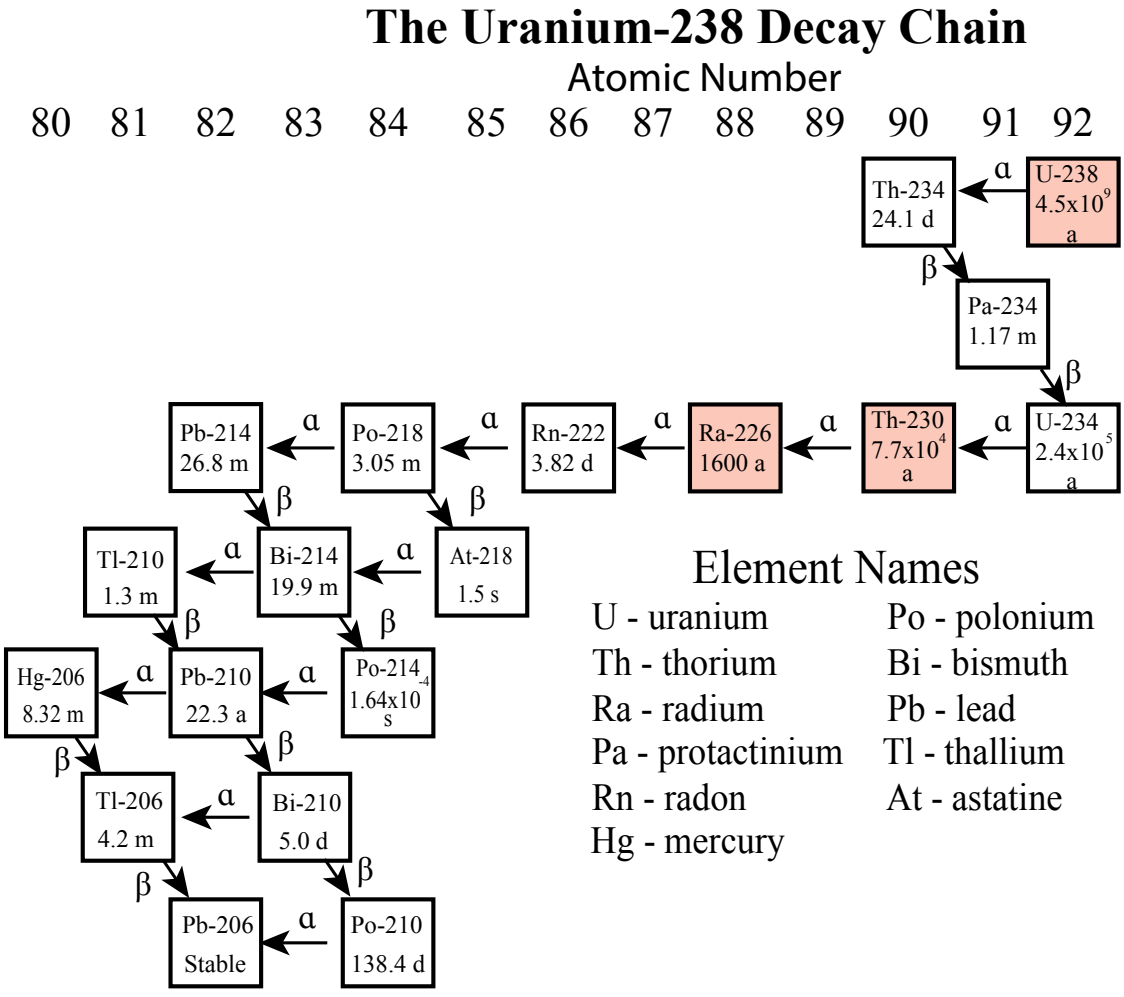

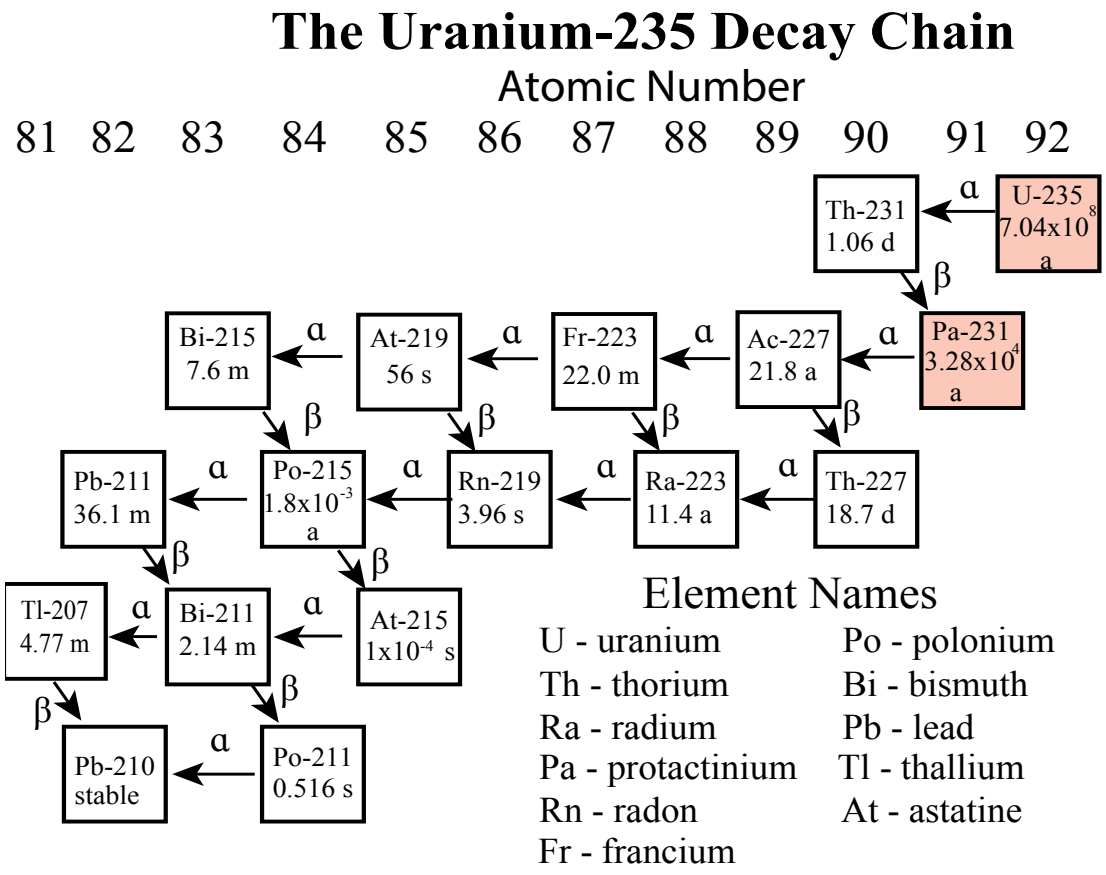

Figure 5. The decay chain of the ^{238}U-series (top) and ^{235}U-series (bottom), after Bourdon et al. (2003). The elements of interest are highlighted in orange.

For this study, I will focus on the decay chains of ^{238}U and ^{235}U, shown in Figure 5. In a decay series, the activity (i.e., nuclides' instantaneous decay rate or $N\lambda$) of radioactive nuclides measures the number of decay events per unit of time (Bourdon et al., 2003; McKenzie, 1985). When a parent nuclide's activity is equal to the activity of a daughter nuclide in the same chain, the system is in secular equilibrium with an activity ratio of 1 (Bourdon et al., 2003; McKenzie, 1985; Spiegelman and Elliott, 1993; Standish and Sims, 2010).

Certain daughter products of the ^{238}U and ^{235}U decay chains are helpful for the analysis of mantle melting because their half-lives resemble the timescales of melting and melt transport processes. For this study, the relevant isotopes are ^{226}Ra, ^{230}Th, and ^{231}Pa. ^{226}Ra (half-life of 1,600 yrs.) helps determine the age of basaltic samples that are otherwise of unknown age, such that higher activity ratios of ($^{226}Ra/^{230}Th$) (i.e., ^{226}Ra excess) constrain eruption ages to five half-lives or < 8000 years (McKenzie, 1985; Russo et al., 2009; Spiegelman & Elliott, 1993; Standish & Sims, 2010; Stracke et al., 2003). ^{231}Pa and ^{230}Th have significantly longer half-lives of 32,800 and 75,000 years, respectively (Bourdon et al., 2003).

The U-series activity ratios between two nuclides of interest within a decay chain (e.g., ($^{230}Th/^{238}U$), ($^{226}Ra/^{230}Th$), and ($^{231}Pa/^{235}U$)) can be disturbed by fractionation processes such as melting and melt-rock chemical interactions, creating a state of disequilibrium and an activity ratio other than 1 (Bourdon et al., 2003; Standish and Sims, 2010). If undisturbed, the system will gradually return to secular equilibrium after ~6 half-lives of the daughter nuclide (Bourdon et al., 2003).

2.2.2 Uranium-series: Effects of mantle heterogeneity

The fractionation of U-Th-Ra during melting is recorded in MORB as disequilibria among the U-series isotopes (Stracke et al., 2006; Russo et al., 2009). For example, melting in the presence of garnet creates ($^{230}Th/^{238}U$) >1 in the partial melt, due to the higher compatibility of U than Th in residual garnet in the presence of silicate melt (Bourdon et al., 1996; Blundy & Wood, 2003; Elkins et al., 2008, 2016, 2019; Lambart et al., 2016; Hirschmann et al., 2003; Hirschmann & Stolper, 1996; Pertermann &

Hirschmann, 2003; Prytulak & Elliott, 2009). A high ($^{230}Th/^{238}U$) activity ratio thus suggests melting of a garnet-bearing lithology, which in the mantle may mean either garnet peridotite or garnet pyroxenite rocks. The pyroxenite scenario, as described above, may provide an explanation for higher melt generation beneath certain mid-ocean ridge segments, leading to higher melt supply to the overlying ridge axis (Blundy & Wood, 2003; Bourdon et al., 1996; Elkins et al., 2019; Lambart et al., 2016 Hirschmann & Stolper, 1996; Wilson et al., 2013).

($^{226}Ra/^{230}Th$) in MORB exhibit a negative correlation with ($^{230}Th/^{238}U$) in age-constrained, unaltered basalts far from hotspots (Sims et al., 2002). This negative correlation has been interpreted to support the continuous melting of a homogeneous mantle source, which progressively evolves while depleting the source in incompatible trace elements (Sims et al., 2002). For example, melting of a homogenous mantle beneath the Kolbeinsey Ridge (i.e., a slow-spreading ridge with thick crust and inferred high potential temperatures) has produced basalts with moderately high ($^{230}Th/^{238}U$) and high ($^{226}Ra/^{230}Th$) and ($^{231}Pa/^{235}U$); these compositions are likely indicative of melting in the garnet lherzolite stability field, without requiring additional mantle heterogeneity (Elkins et al., 2011).

Studies of oceanic basalts from other MOR locations have suggested a significant, measurable contribution of partial melts from garnet pyroxenites and eclogites, however (Elkins et al., 2016, 2019; Lambart et al., 2016; Lyu, 2019; Hirschmann & Stolper, 1996; Hirschmann et al., 2003; Pertermann & Hirschmann et al., 2003; Prytulak & Elliott, 2009). Due to the highly incompatible nature of U-series isotopes during partial melting, very small degrees of melting are expected to fractionate the nuclides from one another.

As explored above, in the presence of garnet, Th is preferentially sequestered into the melt, generating a ($^{230}Th/^{238}U$) activity ratio >1 (Blundy & Wood, 2003; Bourdon et al., 1996; Elkins et al., 2008, 2019). ($^{230}Th/^{238}U$) activity ratios, especially when considered together with ($^{226}Ra/^{230}Th$) and ($^{231}Pa/^{235}U$) activity ratios, are also sensitive to the quantity of garnet in the melting residue and can thus help to fingerprint the difference between deep melting of garnet lherzolite and garnet pyroxenite (Blundy & Wood, 2003; Sims et al., 1999, 2002). Because of their recycled origins, such sources are also expected to have high concentrations of incompatible elements and enriched radiogenic isotope signatures. Enriched radiogenic isotopes, coupled with high ($^{230}Th/^{238}U$) and low ($^{226}Ra/^{230}Th$) and ($^{231}Pa/^{235}U$) excesses, are thus particularly indicative of lithologic heterogeneity of the source, specifically the presence of recycled, pyroxene-rich mafic rocks (Elkins et al., 2011, 2014, 2016b, 2019; Lundstrom et al., 1998b, 1999; Russo et al., 2009; Turner et al., 2015; Waters et al., 2011).

Uranium-series measurements from different segment types along the Mid-Atlantic Ridge may thus assist in evaluating the origins of magma supply variations, in particular, whether melting of more fusible mantle heterogeneities plays a role in the generation of different crustal faulting and accretion styles (Elkins et al., 2019; Klein & Langmuir, 1987; McKenzie, 1985; Spiegelman, 2000; Spiegelman & Elliott, 1993; Strake et al., 2003; Williams & Gill, 1989).

2.3 Melting models

The development of isotopic disequilibrium during continuous reactions like partial melting is complex. Computational models are used to calculate concentrations

and activity ratios of U-series isotopes in partial melts by manipulating variables such as porosity, solid mantle upwelling rates, melt migration rates, solid/liquid partition coefficients, and lithospheric thickness (Lambart et al., 2016; Elkins et al., 2019; McKenzie, 1985; Spiegelman, 2000; Spiegelman & Elliott, 1993; Strake et al., 2003; Williams & Gill, 1989). Changes in these input variables allow model users to compare the sensitivity of U-series disequilibria in partial melts to factors of interest, such as lithologic types, melt extraction mechanisms, and solid decompression rates. Prior studies have developed (e.g., McKenzie, 1985; Spiegelman & Elliott, 1993; Williams & Gill, 1989) and explored the effects of partial melting on U-series nuclides using melting models (e.g., Elkins et al., 2019; Niu et al., 2001; Prytulak & Elliott, 2009). The end-member model scenarios are dynamic melting (e.g., McKenzie, 1985; Williams & Gill, 1989) and RPF (e.g., Navon & Stolper, 1987; Spiegelman & Elliott 1993). Once measured, U-series results from the Kane-Atlantis Supersegment can be compared to the modeling results and may help determine variations of melt supply.

2.3.1 Dynamic melting

One of the first radioactive disequilibrium melting models, dynamic melting, was developed by McKenzie (1985) to track the residence times of U-series isotopes during two-phase (solid and liquid) flow (Figure 6). The dynamic melting model calculates outcomes for a near-fractional (i.e., chemical disequilibrium) melting scenario with a critical melt porosity threshold, above which the melt travels instantaneously in chemical isolation (Bourdon et al., 2003; McKenzie, 1985; Williams & Gill, 1989). The resulting model outcomes typically reveal that incompatible elements are efficiently removed from

the residual source during progressive melting at depth, an expected effect of disequilibrium melt extraction (Blundy & Wood, 2003; McKenzie, 1985; Williams & Gill, 1989). Near-fractional, dynamic melting is also relatively insensitive to variables such as thermal isolation versus thermal re-equilibration between two coexisting lithologies (Elkins et al., 2019). Based on prior calculations and tests, the model is thus primarily sensitive to initial melting conditions (McKenzie, 1985; Richter, 1986; Williams & Gill, 1989) and bulk rock partition coefficients (Elkins et al., 2008; Stracke et al., 2003; Sims et al., 2002; Pertermann & Hirschmann, 2003).

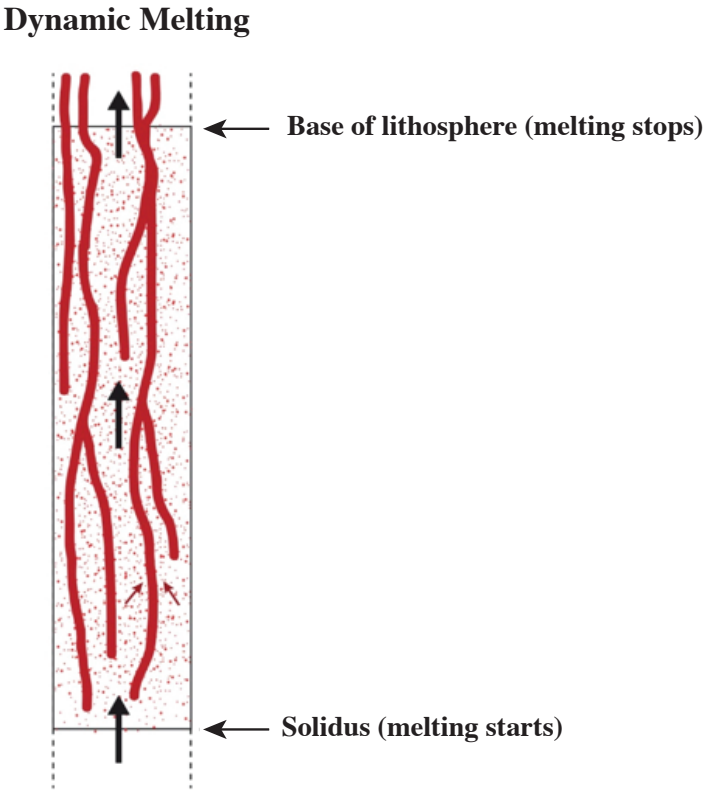

Figure 6. This diagram shows a time-independent mantle upwelling column experiencing dynamic melting after McKenzie (1985), modified from Elkins et al. (2019). The thick red lines are flow paths and indicate the high porosity channels with finite width, and the black arrows indicate magma flow path. The red dots are small degrees of melt residing in the pore space of the host rock.

In dynamic melting scenarios, ^{226}Ra and ^{230}Th excesses relative to their parent nuclides are thus dominantly produced at the bottom of the melt column (i.e., in the garnet lherzolite stability field for higher mantle temperature scenarios) (Blundy & Wood, 2003; Sims et al., 1999, 2002). A result of this outcome is that rapid transport is required to preserve ^{226}Ra-^{230}Th disequilibrium in partial melts, since the extracted accumulated melt cannot react with the solid matrix during ascent and instead simply experiences radioactive decay due to aging during transport (Blundy & Wood, 2003; Sims et al., 1999, 2002). ^{226}Ra excess relative to ^{230}Th is thus best produced and preserved in dynamic melting scenarios with relatively slow melting rates that generate high ($^{226}Ra/^{230}Th$) initially, followed by very fast melt extraction (McKenzie, 1985; Spiegelman & Elliott, 1993; Zou, 1998; Zou & Zindler, 2000). Due to the large range of ($^{226}Ra/^{230}Th$) observed in global oceanic basalts, one of the main constraints on dynamic melting is the rate of extraction needed to preserve ^{226}Ra produced from the bottom of the melt column (Blundy & Wood, 2003; Prytulak & Elliott, 2009; Sims et al., 1999, 2002; Williams & Gill, 1989).

($^{230}Th/^{238}U$) and ($^{231}Pa/^{235}U$) have longer half-lives than ^{226}Ra and are thus most sensitive to the local melt fraction in equilibrium with the matrix, bulk rock partition coefficients, melting rate, and melting time (McKenzie, 1985; Sims et al., 1999; Zou & Zindler, 2000). In comparison, the ($^{226}Ra/^{230}Th$) generated during melting is typically only sensitive to the melt fraction in local equilibrium with the matrix (McKenzie, 1985; Zou & Zindler, 2000), controlled by the residual melt porosity during melting.

Stracke et al. (2006) argued that near-fractional dynamic melting of peridotite mantle explains most observed U-series disequilibria in MORB. The dynamic melting model results of Elkins et al. (2019) argue against purely dynamic melting of peridotite mantle, however, as their ($^{230}Th/^{238}U$) ratio results are too low to explain global MORB data. Their lower ($^{230}Th/^{238}U$) ratios may be due to initial melt productivity variations rather than solely partition coefficients (Elkins et al., 2019).

2.3.2 Reactive porous flow melting

Spiegelman and Elliott (1993) developed an alternative melting model that tracks U-series decay and rock-melt partitioning with full equilibration between the decompressing solid and liquid over time. Their RPF model explicitly calculates the flow of the melt and the solid in continuous chemical interaction in equilibrium and disequilibrium transport scenarios. This chemical interaction generates outcomes where each element effectively travels at different velocities depending on their partitioning (i.e., a chromatographic effect; Spiegelman & Elliott, 1993). As a result, a more compatible parent element travels slower and resides in the melt column for longer, where it decays and increases the quantity of more incompatible daughters via ingrowth, thus considering radioactive decay and conservation of mass (Figure 7) (Blundy & Wood, 2003; McKenzie, 1985; Spiegelman & Elliott, 1993).

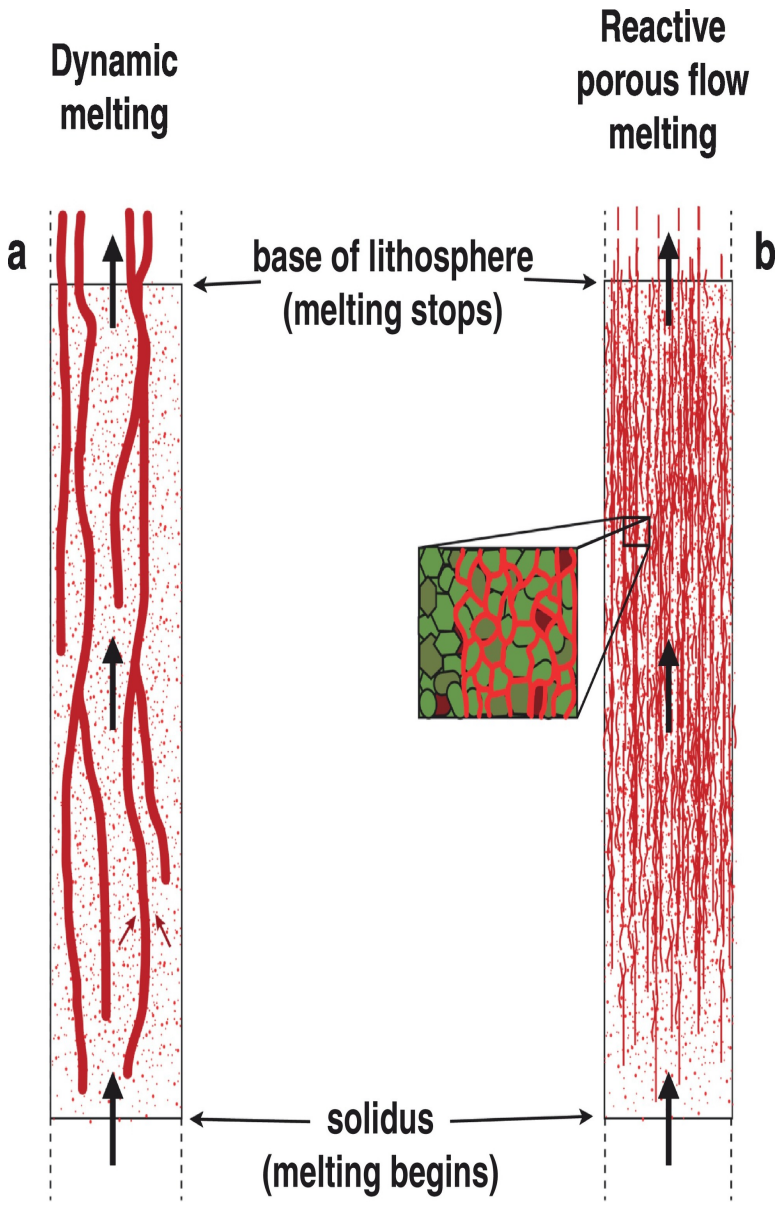

Figure 7. Conceptual diagram from Elkins et al. (2019) and references therein illustrating time-dependent melting scenarios for **a**. dynamic melting and **b**. RPF transport processes. The red specks represent small degrees of melt residing in the pore space of the host rock. The red and black arrows represent magma flow paths. The dynamic melting is the same as in Figure 6. RPF flow paths follow low-porosity grain boundaries (Elkins et al., 2019).

Figure 7 illustrates the differences between dynamic melting and reactive porous flow melting (Elkins et al., 2019). U-series isotopes can be further disturbed when

heterogeneities begin melting in RPF models and is illustrated in Figure 8 (Elkins et al., 2019).

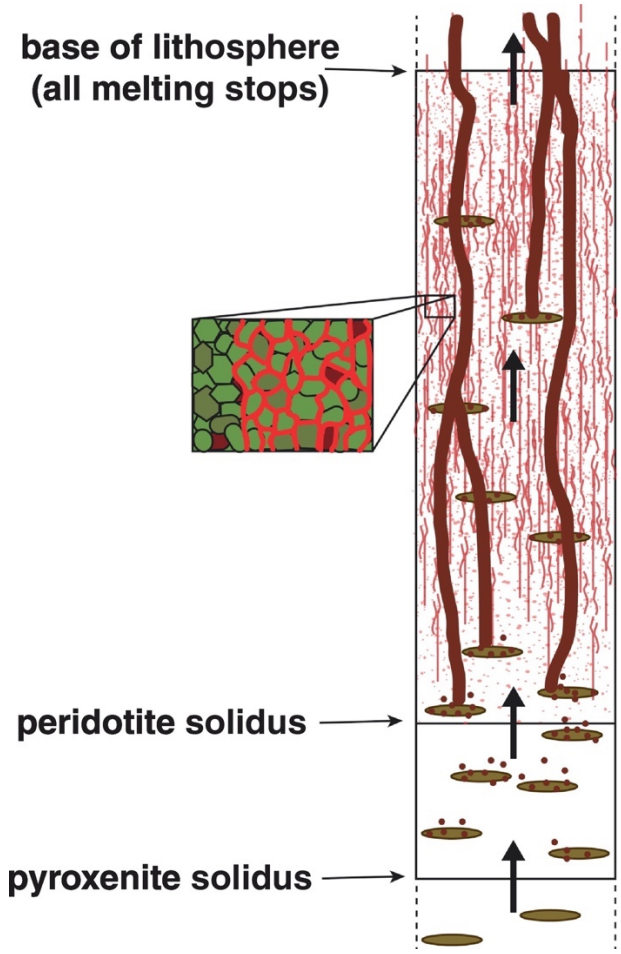

Figure 8. The diagram of the equilibrium transport RPF scenario shows low-porosity flow around grains in a bilithologic melting regime after Elkins et al. (2019). The brown ellipses are fertile pyroxenite zones with deeper onset melting than the ambient peridotite. Melting of pyroxenite starts at the pyroxenite solidus, while melting of peridotite starts at the peridotite solidus. Pyroxenite partial melting is shown by the dark droplets, which later travel by channelized flow. The ambient peridotite melts are shown by the light droplets, which partially melt above the peridotite solidus and flow along the grain boundaries by porous flow. Peridotite droplets that travel via channelized flow would be considered in disequilibrium transport.

Figure 8 illustrates the melt transport mechanisms for RPF equilibrium transport in a bilithologic melting regime, where the partial melt generated above the respective

solidus travels along grain boundaries in a low porosity transport regime (Elkins et al., 2019). In addition to the equilibrium transport described above, the RPF equations can also be used to simulate a disequilibrium scenario where the melt and solid travel in pure chemical disequilibrium (see Spiegelman & Elliott, 1993 appendix). The RPF disequilibrium transport model thus calculates perfect fractional extraction without re-equilibration between the solid and melt and accounts for different ascent times (Blundy & Wood, 2003; Elkins et al., 2019; Elkins & Spiegelman, accepted; Spiegelman & Elliott, 1993). The disequilibrium RPF model is thus similar to true accumulated fractional melting, where the solid only interacts with instantaneous melts in local chemical equilibrium, while accounting for the additional effects of time on melting and melt transport for radioactive nuclides (Elkins et al., 2019; Elkins & Spiegelman, accepted; Navon & Stolper, 1987; Sims et al., 2002; Spiegelman & Elliott, 1993).

In equilibrium RPF melting outcomes, in contrast with dynamic melting, high ($^{226}Ra/^{230}Th$) does not need to be produced at the base of the melt column and then preserved through rapid extraction to be observed in erupted melts; instead, excess ^{226}Ra relative to ^{230}Th can be continually produced throughout the melt column, even with comparatively slow melt migration (Cooper et al., 2000; Sims et al., 1999, 2002; Spiegelman & Elliott, 1993). A numerical calculator that determines U-series outcomes for the disequilibrium transport RPF model (known as “scaled disequilibrium”) and mechanistically resembles dynamic melting, has recently been developed (Elkins & Spiegelman, accepted). This new model has not yet been tested, however, so it is currently unclear how sensitive partial melting outcomes will be to the initial melting rate and melt extraction.

As noted above, lithologic heterogeneities can also cause significant differences in U-series isotopes in modeled basaltic partial melts for both dynamic and equilibrium transport RPF scenarios (e.g., Elkins et al., 2019; McKenzie, 1985; Spiegelman, 2000; Spiegelman & Elliott, 1993; Stracke et al., 2003; Williams & Gill, 1989). Unlike dynamic melting, disequilibrium RPF maintains mass conservation while solving for pure chemical disequilibrium transport, with no continuous chemical reaction between the liquid and the coexisting solid (Elkins & Spiegelman, accepted; McKenzie, 1985; Spiegelman & Elliott, 1993). The outcomes of a RPF disequilibrium model for a bilithologic (i.e., peridotite and pyroxenite) mantle melting scenario are not well studied and require further research.

2.4 Geologic Setting

2.4.1. The Kane-Atlantis Supersegment

Located along the Mid-Atlantic Ridge (MAR) between 24° N-31° N and between the Kane and Atlantis Fracture Zones (Figure 9, Murton & Rona, 2015), the Kane-Atlantis (KA) Supersegment is a long, slow-spreading ridge segment. This segment has a half-spreading rate of less than 1.8 cm/yr and a crustal thickness up to 6 km (Murton & Rona, 2015). Axial depths range from 3450 m in the north to 4400 m in the south and have inferred corresponding mantle temperature variations of ~83°C, with higher temperatures in the north (towards the Azores hotspot) (Murton & Rona, 2015). Although the underlying mantle lithology and the relative contribution of pyroxenite partial melts to basaltic magmas produced beneath the KA Supersegment axis remain unclear, the morphology and seismicity of the area are well-characterized (Blackman et al., 1998,

2009; deMartin et al., 2007; Murton & Rona, 2015). The KA Supersegment is subdivided into thirteen smaller, second-order segments divided by a combination of transform faults and non-transform offsets (Murton & Rona, 2015; Olive & Escartín, 2016). The axial valleys of these smaller segments, some of which expose lower crust and upper-mantle lithologies along fault surfaces, are bounded by a combination of typical normal faults as well as detachment faults (Murton & Rona, 2015).

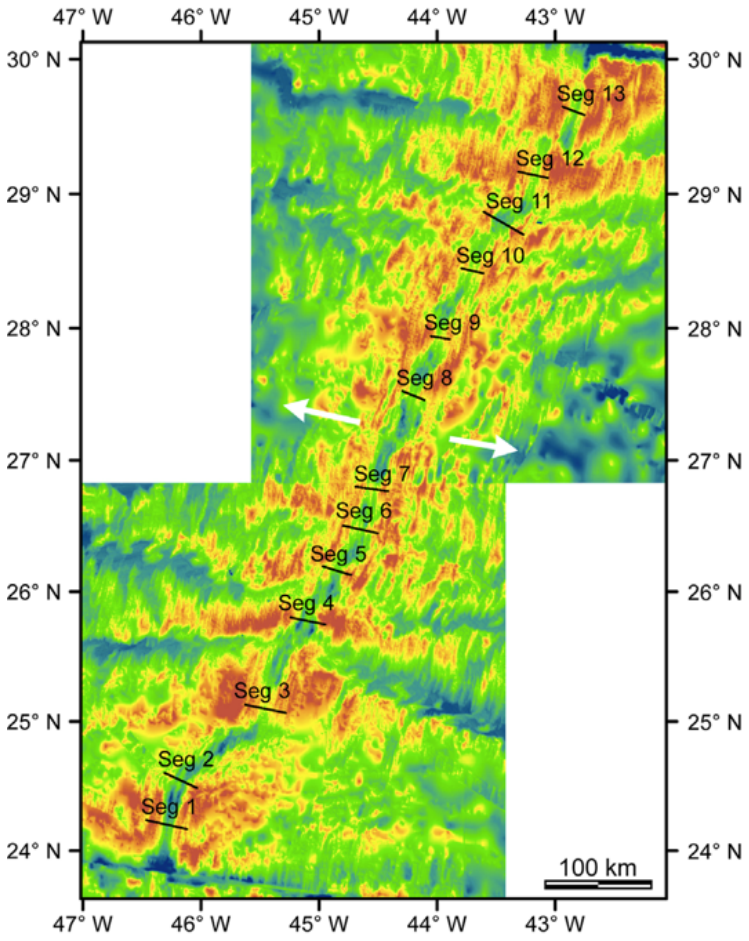

Figure 9. Bathymetric map of the Kane-Atlantis Supersegment, red representing shallower seafloor depths and blue greater depths. The white arrows indicate spreading direction of the plates (Murton & Rona, 2015). The global location map of the KA Supersegment is seen in Figure 1. The Kane Megamullion from Figure 2 is outside of the study area at 23°30'N and 45°16'W.

The outer segments (segments 1 and 13; Figure 9) have pronounced inside corner highs along the adjacent fracture zones, with relatively thin, magma-starved crust (Murton & Rona, 2015; Olive & Escartín, 2016). Segment 4 hosts a dispersed hydrothermal field (the Trans-Atlantic Geotraverse, or TAG) and is interpreted to overlie a buried detachment surface that has been imaged seismically (deMartin et al., 2007; Humphris et al., 2015a; MacLeod, 2009; Murton & Rona, 2015; Olive & Escartín, 2016).

Other second-order segments exhibit more symmetrical spreading geometry, while still others appear to be spreading moderately obliquely to the ridge axis and thus exhibit a distinct type of oblique asymmetry (Abelson & Agnon, 1997). More broadly, approximately 50% of the MAR likely hosts detachment fault-bearing second-order segments, and based on seafloor morphology, exposed fault surfaces, and seismic evidence, the KA Supersegment appears to host at least 6 detachment fault-bearing segments (Humphris et al., 2015 b; McLeod et al., 2009; Murton & Rona, 2015; Tucholke et al., 1998, 2008).

The Kane-Atlantis Supersegment thus has a consistent spreading rate, nearly constant and monotonically varying axial depth and crustal thickness, and many second-order segments with distinct spreading characteristics. The KA Supersegment has also been extensively mapped and sampled through multiple expeditions. These characteristics make the KA Supersegment a valuable area for studying magma supply and crustal accretion that influence divergent tectonic properties along slow-spreading mid-ocean ridges.

The major and trace element data from Lyu (2019) is part of the larger study of how melt supply under the second order segments of the KA Supersegment effects the

local sea floor symmetry. Using U-series models to simulate outcomes of partial melting of pyroxenite and peridotite using varying lithospheric caps might provide insight into how melt transport and supply might affect U-series activity ratios measured in erupted basalts. These U-series model results might be applied to future U-series measurements of the KA Supersegment in combination with the major and trace element data of Lyu (2019) to determine how mantle heterogeneities affect crustal accretion and sea floor symmetry.

3. Methods

3.1 Model rationale

3.1.1 Model Background and Software

As explored above, a number of questions remain regarding the generation of partial melts in the sub-oceanic mantle. Uranium-series isotopes are particularly sensitive to the timing and mechanisms of partial melting and melt transport, but the interpretation of U-series isotope data in oceanic basalts is complex and requires numerical modeling methods. In particular: 1) oceanic lithospheric thickness and 2) partial melting of a heterogeneous mantle source is expected to have a noticeable, measurable effect on the U-series isotopes (Elkins et al., 2019), but the results of melting under different magma migration circumstances and the sensitivity of U-series disequilibria to those variables remains unclear. Here I have developed a series of preliminary model calculation tests to explore and better characterize the influence of lithospheric thickness and bilithologic melting on U-series partial melt compositions.

Specifically, I used the pyUserCalc model (in a Jupyter Notebook program) to calculate U-series disequilibria in partial melts, for both equilibrium and disequilibrium porous flow transport scenarios. The pyUserCalc code uses numerical methods to model RPF in a 1-D, decompressing mantle melt column (Elkins & Spiegelman, accepted), similar to the older UserCalc program (Spiegelman, 2000). The model calculations find solutions to RPF equilibrium and disequilibrium transport equations from Spiegelman and Elliott (1993) to calculate U-series disequilibria in partial melts. The new numerical solution to disequilibrium transport melting developed by Elkins and Spiegelman (accepted) is controlled by mass conservation and uses the Damköhler number (*Da*) to simulate a complete fractional melting scenario (Da=0). The pure equilibrium transport melting model simulates a scenario where Da=∞ and relies on the simpler equilibrium porous flow equations of Spiegelman & Elliott (1993) with Spiegelman's (2000) numerical solution approach.

In more detail, Spiegelman & Elliott (1993) developed an equilibrium transport model that accounts for the conservation of mass for both melt and solid phases, for each nuclide of interest in the decay chain and a 1-D steady-state model (after formula 6 in Spiegelman, 2000):

$$\frac{dc_i^f}{dz} = \frac{-c_i^f(z)}{F(z) + \big(1 - F(z)\big)D_i(z)} \frac{d}{dz}\big[F(z) + \big(1 - F(z)\big)D_i(z)\big] \qquad (1)$$

$$+ \frac{\lambda_{i-1}\rho_f D_{i-1} c_{i-1}^f(z) - \lambda_i \rho_f D_i c_i^f(z)}{\rho_s W_0 [F(z) + \big(1 - F(z)\big)D_i(z)]}$$

where c_i is the concentration of element or nuclide *i* in the fluid *(f)*, *F(z)* is the melt fraction as a function of depth *(z)*, $D_i(z)$ is the bulk solid/melt partition coefficient for element *i* as a function of depth, l_i is the decay constant for element *i*, *r* is the density of the fluid *(f)* or solid *(s)*, W_0 is the one-dimensional solid upwelling rate, and *(i-1)* indicates the parent of nuclide *i*. The first of the two terms on the right-hand side of eq (1) track the changes in concentration of nuclide *i* with solid and melt partition coefficients in a true batch melting scenario, independent of porosity and upwelling. The last term tracks the concentration due to radioactive ingrowth and decay, and is a function of the residual melt porosity and the solid mantle upwelling rate (Spiegelman, 2000; Spiegelman & Elliott, 1993). The numerical model solves for the log of the concentration U_i as opposed to nuclide concentrations because U_i is more accurate for highly incompatible elements (Spiegelman, 2000). Issues occur when there is an extreme change in the solid concentrations of highly incompatible elements, causing the ODE solver to find unstable solutions at low values (Elkins & Spiegelman, accepted). The log of the concentration U_i is defined in equations (2-4) below (formulas (7-9) in Spiegelman, 2000):

$$U_i^f = ln\left(\frac{c_i^f}{c_{i,0}^f}\right) \tag{2}$$

with

$$\frac{dU_i^f}{dz} = \frac{1}{c_i^f(z)}\frac{dc_i^f}{dz} \tag{3}$$

to produce

$$\frac{dU_i^f}{dz} = \frac{-1}{F(z) + \big(1 - F(z)\big)D_i(z)} \frac{d}{dz}\big[F(z) + \big(1 - F(z)\big)D_i(z)\big] \qquad (4)$$

$$+ \frac{\lambda_i}{w_{eff}^i}\big[R_i^{i-1} \exp\big[U_{i-1}^f(z) - U_i^f(z)\big] - 1\big]$$

where the log concentration of nuclide *i* in the melt, $U_i(z)$ in the fluid *(f)*, decomposes into stable and radioactive parts such that $U_i(z) = U_i^{stable}(z) + U_i^{rad}(z)$. $U_i^{rad}(z)$ is the radiogenic ingrowth component, w_{eff} is the effective liquid velocity, R_i^{i-1} is the ingrowth factor, and $c_{i,0}^f$ is the concentration of element or nuclide *i* in the fluid *(f)* at secular equilibrium (formula (15) from Elkins & Spiegelman, accepted).

As described above, Spiegelman and Elliott (1993) also solved for RPF with chemical disequilibrium melt transport. The disequilibrium transport model is similar to the above equations. However, the solid produces an instantaneous melt fraction that is only in local equilibrium with the solid and does not react with the solid matrix further during transport, such that Da=0 (Elkins & Spiegelman, accepted; Spiegelman & Elliott, 1993).

For this study, melting was calculated for a decompressing solid experiencing both pure equilibrium and pure disequilibrium transport. The model scenario was stopped at the base of the lithosphere, to simulate purely asthenospheric melting and calculate the U-series disequilibria resulting from decompression and partial melting alone. In the second round of calculations, these resulting partial melt compositions were then modified to determine the further effects of radioactive decay, to simulate simple magma transport and aging through the overlying oceanic lithosphere. The two rounds of calculations were determined for multiple lithospheric thicknesses and two different types

of mantle pyroxenite coexisting with peridotite. The second transport aging/decay calculation was determined using a second Jupyter notebook tool (Elkins & Lambart, in prep.). This calculation uses U-series radioactive decay equations to determine the effects of aging during melt transport through the lithosphere without further chemical interaction (from decay equations in Zou, 2007).

3.1.2 Modeling variables

Using the models presented above, I explored how lithospheric caps at 10 kbar and 15 kbar (i.e., depths of 30 km and 46 km, respectively) affect the U-series disequilibrium compositions of partial mantle melts (Hirschmann et al., 2003; Niu et al., 1997; Pierce et al., 2019; Salters & Stracke, 2004; Yaxley & Sobolev, 2007). Lithospheric thicknesses of 30 km and 46 km are in the mid-range of thicker oceanic lithosphere (i.e., between mid-ocean ridges and ocean island lithospheric thickness; after Hole & Millet, 2016) and might represent thicker oceanic lithosphere at slow-spreading ridges. I used the bilithologic melting methods of Elkins et al. (2019) and pyUserCalc to solve and generate gridded results of RPF equilibrium and disequilibrium transport model calculations (Elkins & Spiegelman, accepted). I calculated the U-series activity ratios in partial melts of MIX1G and Gb-108 pyroxenites and a coexisting peridotite. These modeling results could be used with U-series measurements and major and trace elements from slow-spreading MOR such as the Kane-Atlantis Supersegment to constrain mantle heterogeneities. The two decompressing lithologies exchange energy to maintain a state of thermal equilibrium while melting before and during lithospheric decay. I used a mantle potential temperature of 1300 ^{o}C, as this is within the expected temperature range

in the mantle under mid-ocean ridges (Asimow et al., 2001; Elkins et al., 2019; Ghiorso et al., 2002; Grose & Afonso, 2013; Herzberg, 2004; Langmuir et al., 1992; McKenzie & Bickle, 1988).

MIX1G pyroxenite is a silica-deficient variety, thought to be representative of an average garnet pyroxenite (Hirschmann et al., 2003; Kogiso et al., 2003), while Gb-108 pyroxenite is a silica-excess variety that resembles a typical olivine gabbro rock (Yaxley & Sobolev, 2007). One or both pyroxenite types (silica excess and silica deficient) may exist in the convecting mantle as products of crustal recycling and mantle mixing processes (e.g., Elkins et al., 2019; Lambart et al., 2016). The coexisting mantle peridotite composition is based on a typical depleted mantle (DM) after Salters & Stracke's (2004) calculated estimate. These compositions were selected to test the respective melting characteristics of lithologies that likely exist in the convecting sub-oceanic asthenosphere and to make a direct comparison to earlier dynamic melting calculations from Elkins et al. (2019).

Petrologic melting constraints (liquid fractions and residual mineral compositions and modes as a function of depth) were based on calculated results from pMELTS and Melt-PX modeling tools (Elkins et al., 2019; Ghiorso et al., 2002; Lambart et al., 2016). The pMELTS tool is used to predict mineral modes while the Melt-PX software predicts near-solidus temperatures and extents of melting as a function of pressure and temperature for pyroxenites (Elkins et al., 2019; Ghiorso et al., 2002; Lambart et al., 2016). For the pressure-temperature paths followed by the melting lithologies, thermal equilibration was assumed between the coexisting pyroxenite and peridotite in a chemically isolated, bi-lithologic mantle (Elkins et al., 2019 and references therein;

Lambart, 2016). Bulk rock partition coefficients for the elements of interest (U, Th, and Ra) were determined using constant mineral/melt partitioning values predicted by the experimental literature (see Appendix A, Table S1 and references therein) and the predicted residual mineral modes from the petrologic calculations above.

Partition coefficients for U and Th in mantle minerals depend on mineral composition, and slight differences in bulk partition coefficients of U and Th can cause significant differences in modeling results (e.g., Bourdon et al., 2003; Elkins et al., 2008, 2011, 2016, 2019; Sims et al., 1999, 2002; Williams & Gill, 1989). Although experimental constraints on compositional dependence are limited, to achieve the most accurate results possible, the partition coefficients used in Elkins et al. (2019) and reproduced in this study were selected considering: 1) the similarity of the melting experimental lithology to our compositions of interest; 2) experiments that reached equilibrium at pressure conditions of interest; 3) experiments where several solids grew together in equilibrium (i.e., clinopyroxene and garnet); and 4) experiments that maintained reasonable oxygen fugacity conditions, which can affect U behavior (Appendix A, Table S1; Elkins et al., 2019 and references therein).

As noted above, the calculated melting column was truncated at a defined base of the lithosphere, P_{Lithos} (at 10 and 15 kbar). Initial model conditions assumed that nuclides of ^{238}U, ^{230}Th, ^{226}Ra, and ^{231}Pa began in secular equilibrium, as expected for typical asthenospheric mantle rocks, due to mantle rock ages likely significantly greater than 500,000 yrs (McKenzie, 1985; Spiegelman & Elliott, 1993; Standish & Sims, 2010).

Uranium-series melt compositions were determined for solid mantle upwelling rates from 0.5 - 10.0 cm/yr and maximum residual melt porosities between 0.1-2.0 %,

similar to previous literature (Elkins et al., 2019; Elkins & Spiegelman, accepted; Grose & Afonso, 2019; Spiegelman, 2000; Zou & Zindler, 2000), simulating a range of possible mid-ocean ridge melting environments. Additional model input variables are shown in Table 1.

Table 1. List of variables used in model calculations. The parameters below were used per the discussion above, previous model runs by Elkins et al. (2019) and references therein.

Variables	Values
P_{lithos}	10, 15 kbar
P_{crust}	2.2 kbar
define_lith_Ds	new
data input option	no lith
φ_0	0.008
W_0	2.5 cm/yr
n	2
ρ_s	3300 kg/m^3
ρ_f	2800 kg/m^3
Initial activity values	1.0 for all
Da (for disequilibrium)	1.00E-10
Depth	P_{lithos}*3.08899
Lithospheric transport rate	1500 cm/yr
Isotopic decay through lithosphere	yes
Batch Operations	
φ_0	0.001, 0.002, 0.005, 0.01, 0.02
W_0	0.5, 1.0, 1.5, 2.0, 4.0, 6.0, 10.0 (cm/yr)

4. Results

Compositions at the base of the lithosphere at 10 kbar and 15 kbar (i.e., where the melting column is truncated), prior to additional transport and decay through the lithospheric layer, represent the maximum possible ratios in the primary melts (Figures 10, 12, 14, 16). Considering the age effects through the lithosphere using a rough estimate for transport rate gives additional insight into how the U-series activity ratios may look upon eruption (Figures 11, 13, 15, 17). The lithospheric transport decay calculation relies on an estimated magma transport rate of 1500 cm/yr. This calculation does not account for other possible processes that could occur, however, such as variations in the magma's path through the lithosphere, time spent pooling in lower crustal crystal mush zones, and melt-rock chemical interactions.

Figures 10 and 12 are the gridded results for the RPF equilibrium transport model calculations for lithospheric caps at 10 kbar (Figure 10) and 15 kbar (Figure 12), after melting stops, but prior to any lithospheric transport with additional radioactive decay. Each melting grid generates outcomes for a series of constant solid mantle upwelling rates (W_0 values) or reference porosities (maximum residual melt porosity values expressed as a mass percent, f). Figures 11 and 13 generate the same gridded results, but after decay through the lithosphere for lithospheric caps of 10 kbar (Figure 11, for a total elapsed decay interval of 2059 yrs.) and 15 kbar (Figure 13, for a decay interval of 3088 yrs.). The decay intervals of 2059 and 3088 years are the transport time intervals corresponding to the thickness of each lithospheric cap, using the same lithospheric transport rate of 1500 cm/yr.

When analyzing the gridded results, a few key points should be considered. The solid lines show model results for constant solid mantle upwelling rates (W), and the dashed lines show outcomes for constant maximum residual porosity values (ϕ) for both ($^{226}Ra/^{230}Th$) versus ($^{230}Th/^{238}U$) and ($^{231}Pa/^{235}U$) versus ($^{230}Th/^{238}U$). For faster upwelling speeds, lower ($^{230}Th/^{238}U$) values should be generated. Upwelling speeds over 2.0 cm/yr do not represent the MOR setting of interest well, but provide a robust range to model over. Per the discussion above, porosity changes mainly affect the ($^{226}Ra/^{230}Th$) and ($^{231}Pa/^{235}U$) values, which should be generated due to the element travel time. The generated porosity results will also be different in the RPF equilibrium and disequilibrium models due to the differences in the calculations of the melt transport discussed in the previous sections.

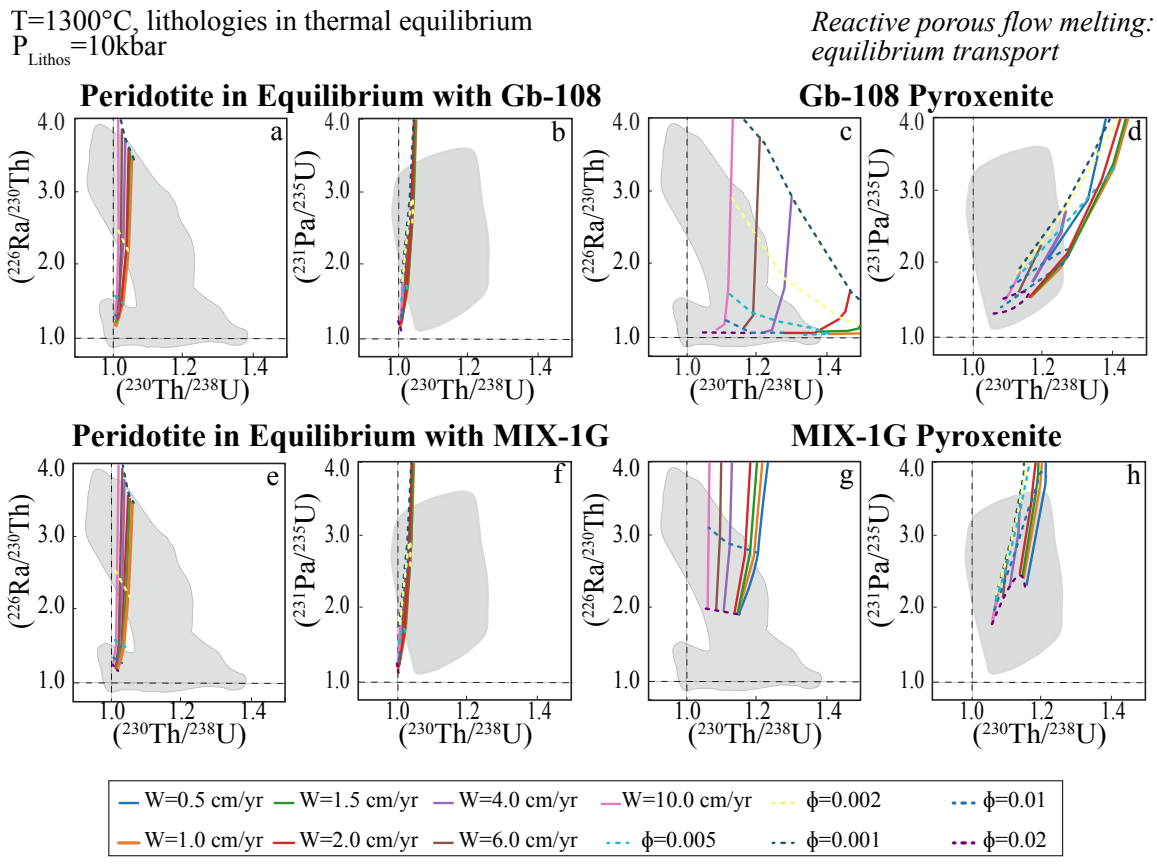

Figure 10. Gridded results for RPF equilibrium transport melting calculations where T=1300°C, the lithospheric cap (P_{Lithos}) is 10 kbar, and peridotite and pyroxenite are in thermal equilibrium. Each grid generates a plot for the ($^{226}Ra/^{230}Th$) versus ($^{230}Th/^{238}U$) and ($^{231}Pa/^{235}U$) versus ($^{230}Th/^{238}U$). The solid lines show model results for constant solid mantle upwelling rates (W), and the dashed lines show outcomes for constant maximum residual porosity values (ϕ). Global MORB data are shown as grey data fields (Bourdon et al., 1996; Bourdon et al., 2000; Cooper et al., 2003; Elkins et al., 2011; Elkins et al., 2014; Elkins et al., 2016; Goldstein et al., 1989; Goldstein et al., 1992; Goldstein et al., 1993; Kokfelt et al., 2003; Lundstrom et al., 1995; Lundstrom et al., 1998a; Lundstrom et al., 1999; Peate et al., 2001; Reagan et al., 2017; Rubin et al., 2005; Russo et al., 2009; Sims et al., 2002; Standish and Sims, 2010; Tepley et al., 2004; Turner et al., 2015; Turner et al., 2016; Waters et al., 2011; Waters et al., 2013). **a.** ($^{226}Ra/^{230}Th$) and **b.** ($^{231}Pa/^{235}U$) versus ($^{230}Th/^{238}U$) for partial melts of peridotite in thermal equilibrium with Gb-108 pyroxenite; **c.** ($^{226}Ra/^{230}Th$) and **d.** ($^{231}Pa/^{235}U$) versus ($^{230}Th/^{238}U$) for partial melts of Gb-108 pyroxenite; **e.** ($^{226}Ra/^{230}Th$) and **f.** ($^{231}Pa/^{235}U$) versus ($^{230}Th/^{238}U$) for partial melts of peridotite in equilibrium with MIX-1G pyroxenite; and **g.** ($^{226}Ra/^{230}Th$) and **h.** ($^{231}Pa/^{235}U$) versus ($^{230}Th/^{238}U$) for partial melts of MIX-1G pyroxenite, all after Elkins et al. (2019).

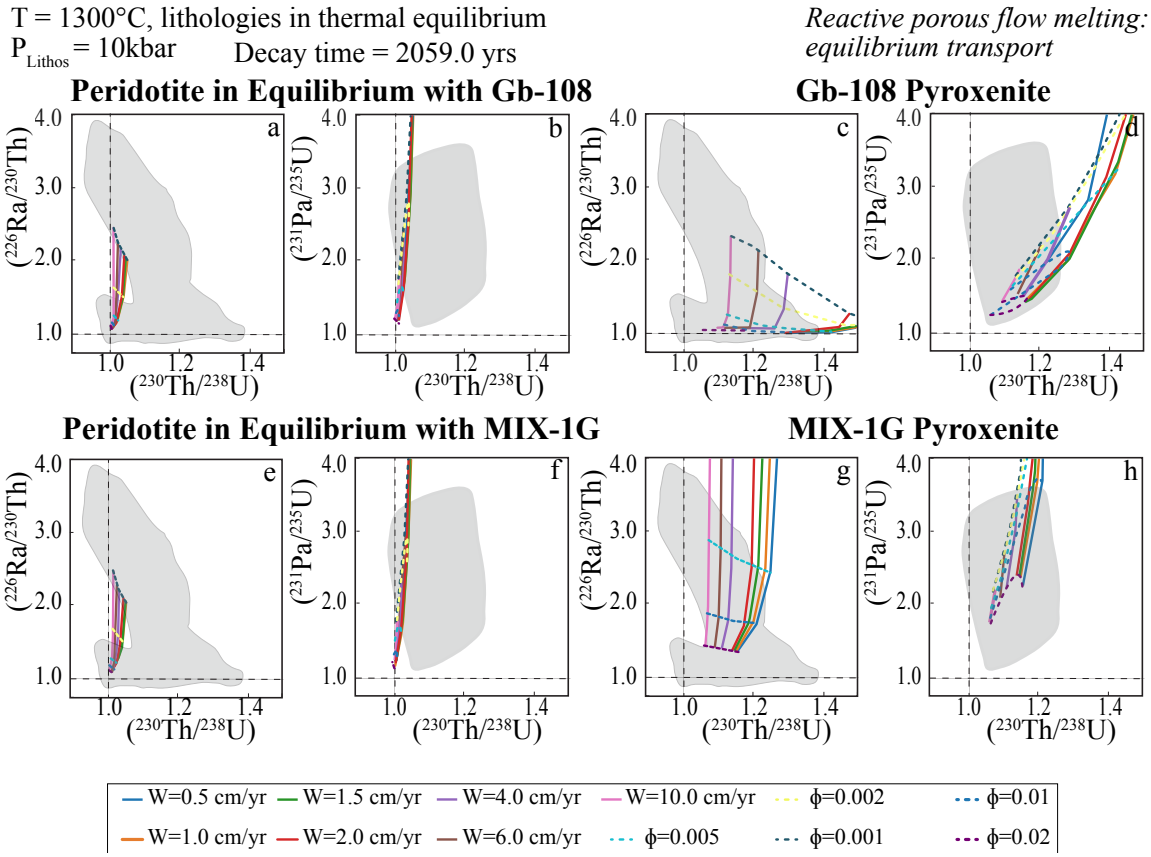

Figure 11. Gridded results for RPF equilibrium transport melting calculations where T = 1300°C, the lithospheric cap (P_{Lithos}) is 10 kbar, a decay time of 2059.0 years, and peridotite and pyroxenite are in thermal equilibrium. The solid lines show partial melting outcomes with constant solid mantle upwelling rates (W), and the dashed lines show outcomes for constant maximum residual porosity values (ϕ). Panels and fields are as described in Figure 10.

T = 1300°C, lithologies in thermal equilibrium
P_{Lithos} = 15kbar

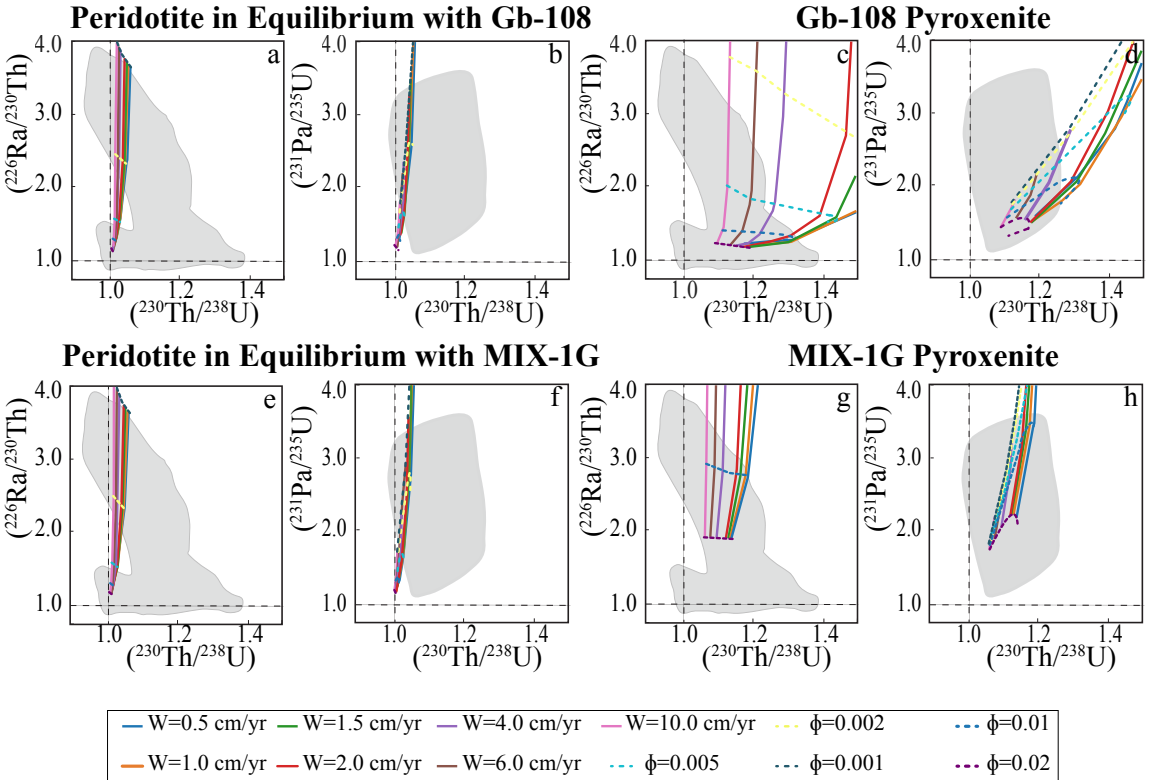

Figure 12. Gridded results for RPF equilibrium transport melting calculations where T = 1300°C, the lithospheric cap (P_{Lithos}) is 15 kbar, and peridotite and pyroxenite are in thermal equilibrium. The solid lines show partial melting outcomes with constant solid mantle upwelling rates (W), and the dashed lines show outcomes for constant maximum residual porosity values (ϕ). Panels and fields are as described in Figure 10.

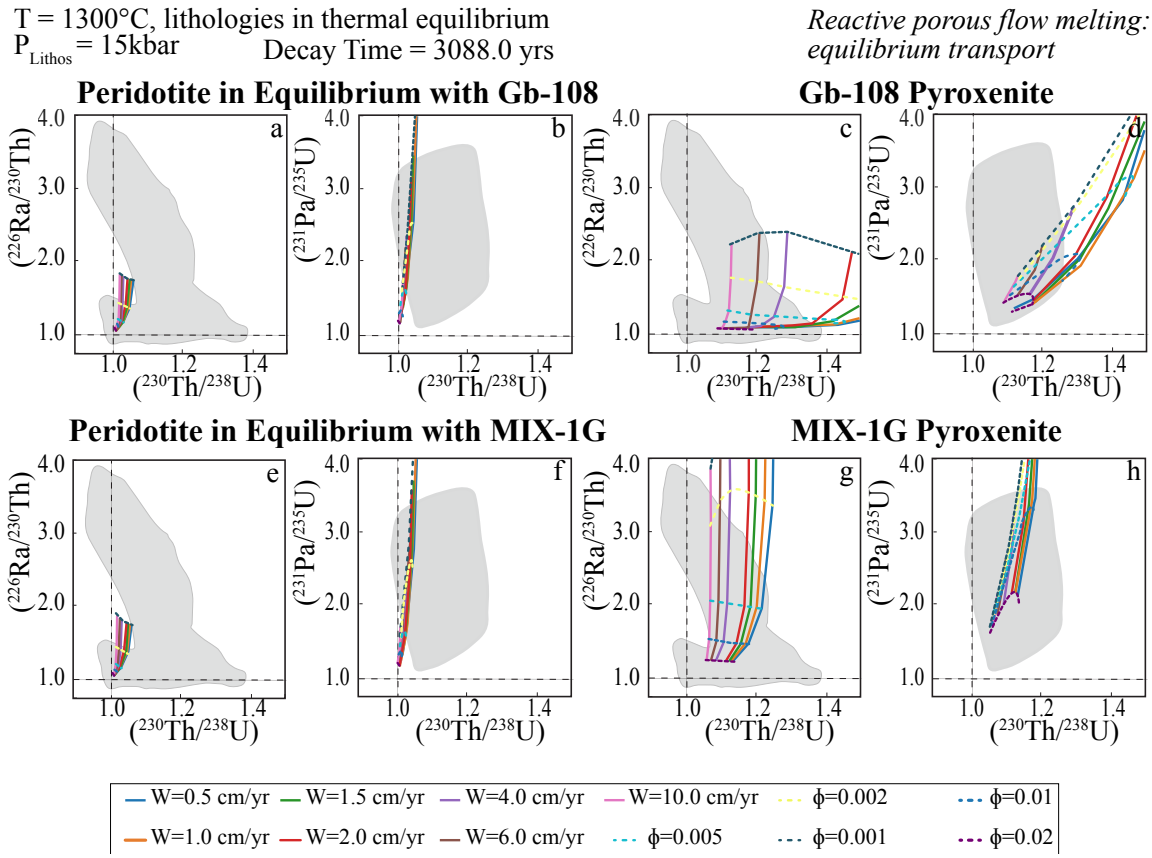

Figure 13. Gridded results for RPF equilibrium transport melting calculations where T = 1300°C, the lithospheric cap (P_{Lithos}) is 15 kbar, a decay time of 3088.0 years, and peridotite and pyroxenite are in thermal equilibrium. The solid lines show partial melting outcomes with constant solid mantle upwelling rates (W), and the dashed lines show outcomes for constant maximum residual porosity values (ϕ). Panels and fields are as described in Figure 10.

Figures 14 and 16 show the gridded results from the RPF disequilibrium transport model calculations after melting stops at 10 kbar (Figure 14) and 15 kbar (Figure 16). Figures 15 and 17 likewise show the gridded results for the same calculations after decay through the lithosphere of 10 kbar (Figure 15, 2059 yrs.) and 15 kbar (Figure 17, 3088 yrs.).

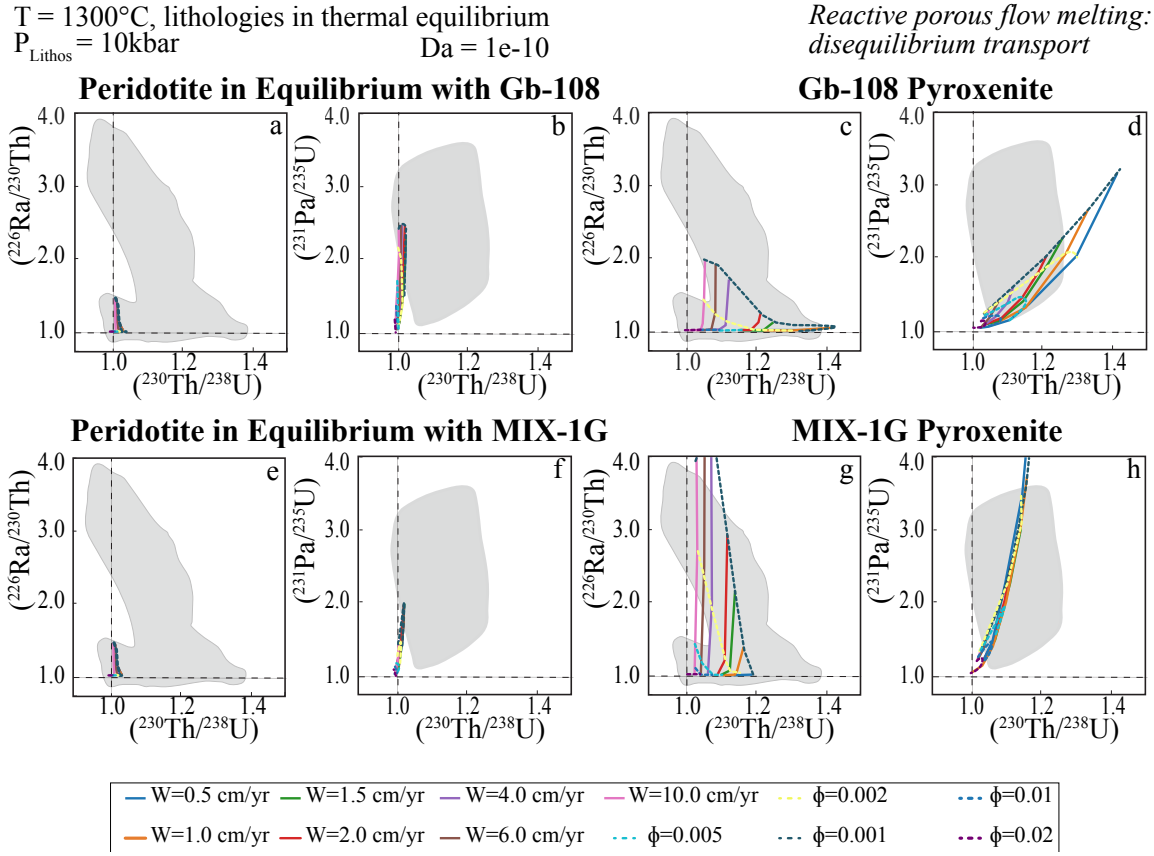

Figure 14. Gridded results for RPF disequilibrium transport melting calculations where T = 1300°C, the lithospheric cap (P_{Lithos}) is 10 kbar, the Damköhler number = 1 x 10^{-10}, and peridotite and pyroxenite are in thermal equilibrium. The solid lines show partial melting outcomes with constant solid mantle upwelling rates (W), and the dashed lines show outcomes for constant maximum residual porosity values (ϕ). Panels and fields are as described in Figure 10.

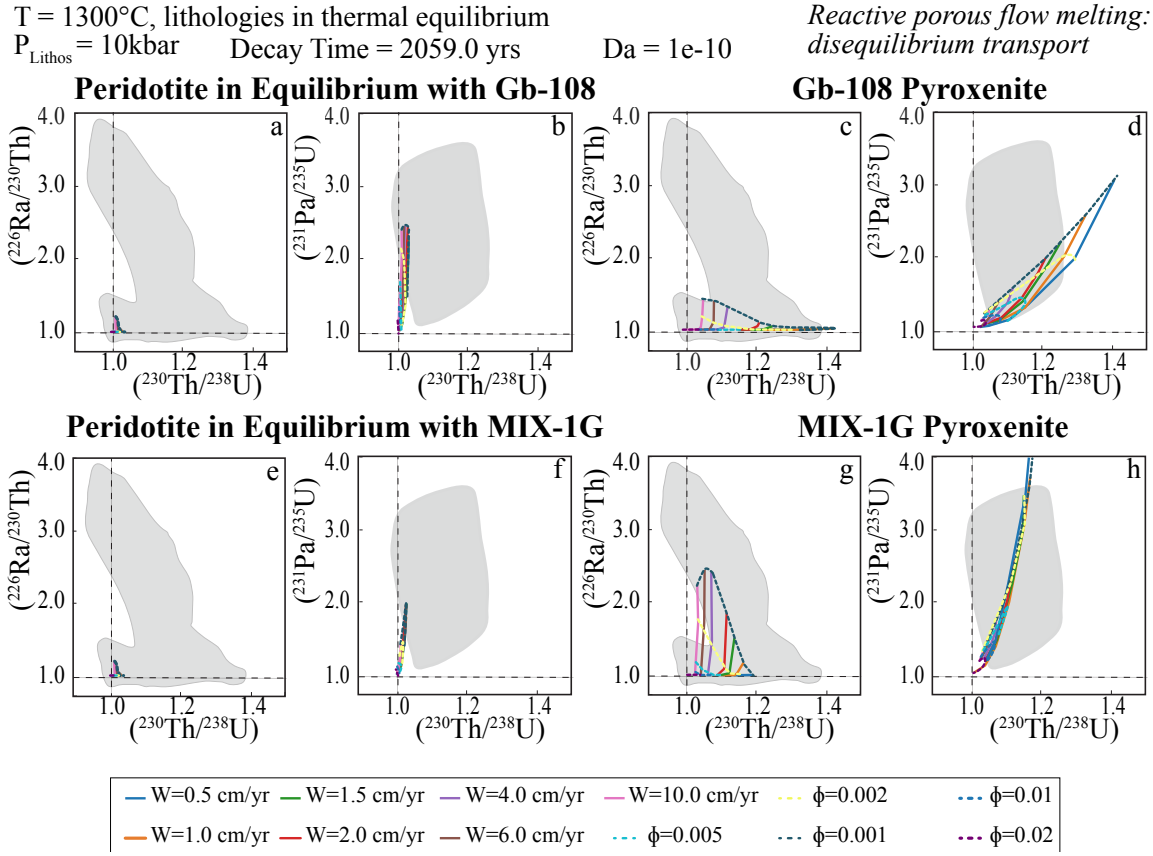

Figure 15. Gridded results for RPF disequilibrium transport melting calculations where T = 1300°C, the lithospheric cap (P_{Lithos}) is 10 kbar, the Damköhler number = 1 x 10^{-10}, a decay time of 2059.0 years, and peridotite and pyroxenite are in thermal equilibrium. The solid lines show partial melting outcomes with constant solid mantle upwelling rates (W), and the dashed lines show outcomes for constant maximum residual porosity values (ϕ). Panels and fields are as described in Figure 10.

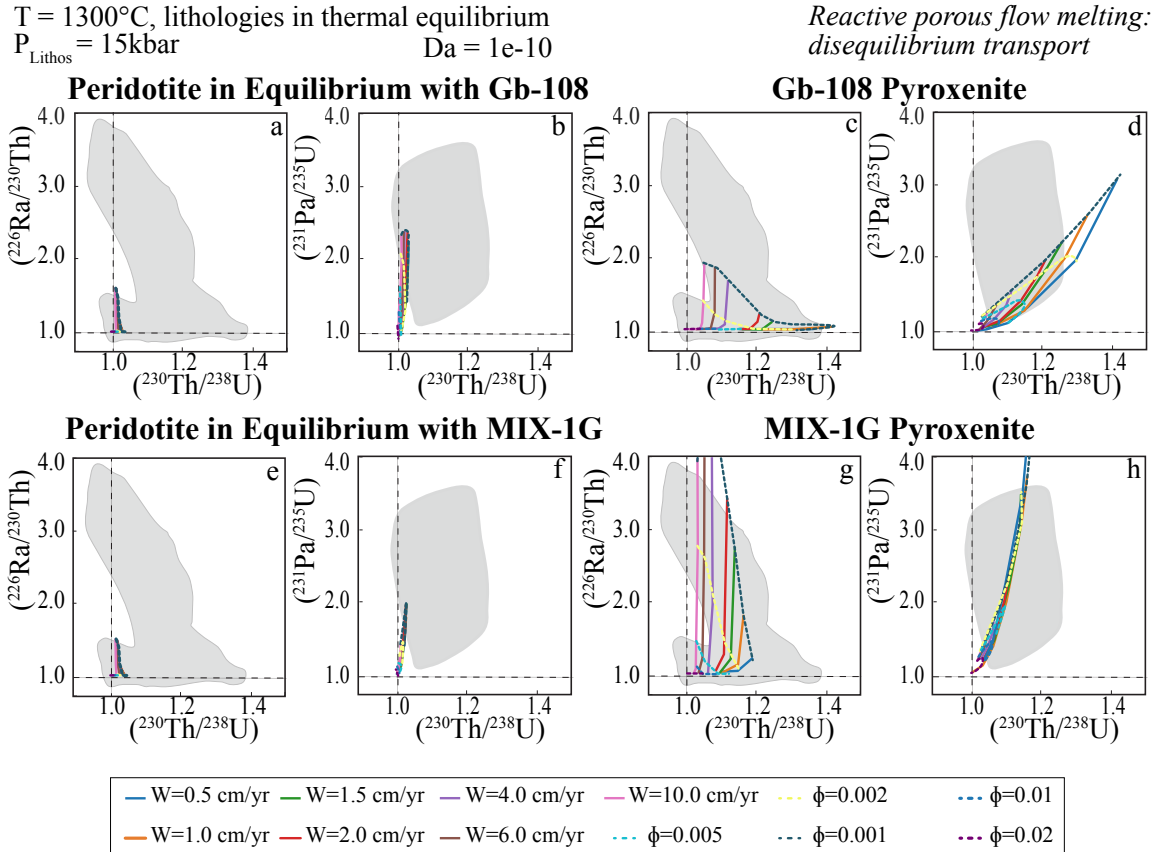

Figure 16. Gridded results for RPF disequilibrium transport melting calculations where T = 1300°C, the lithospheric cap (P_{Lithos}) is 15 kbar, the Damköhler number = 1 x 10^{-10}, and peridotite and pyroxenite are in thermal equilibrium. The solid lines show partial melting outcomes with constant solid mantle upwelling rates (W), and the dashed lines show outcomes for constant maximum residual porosity values (ϕ). Panels and fields are as described in Figure 10.

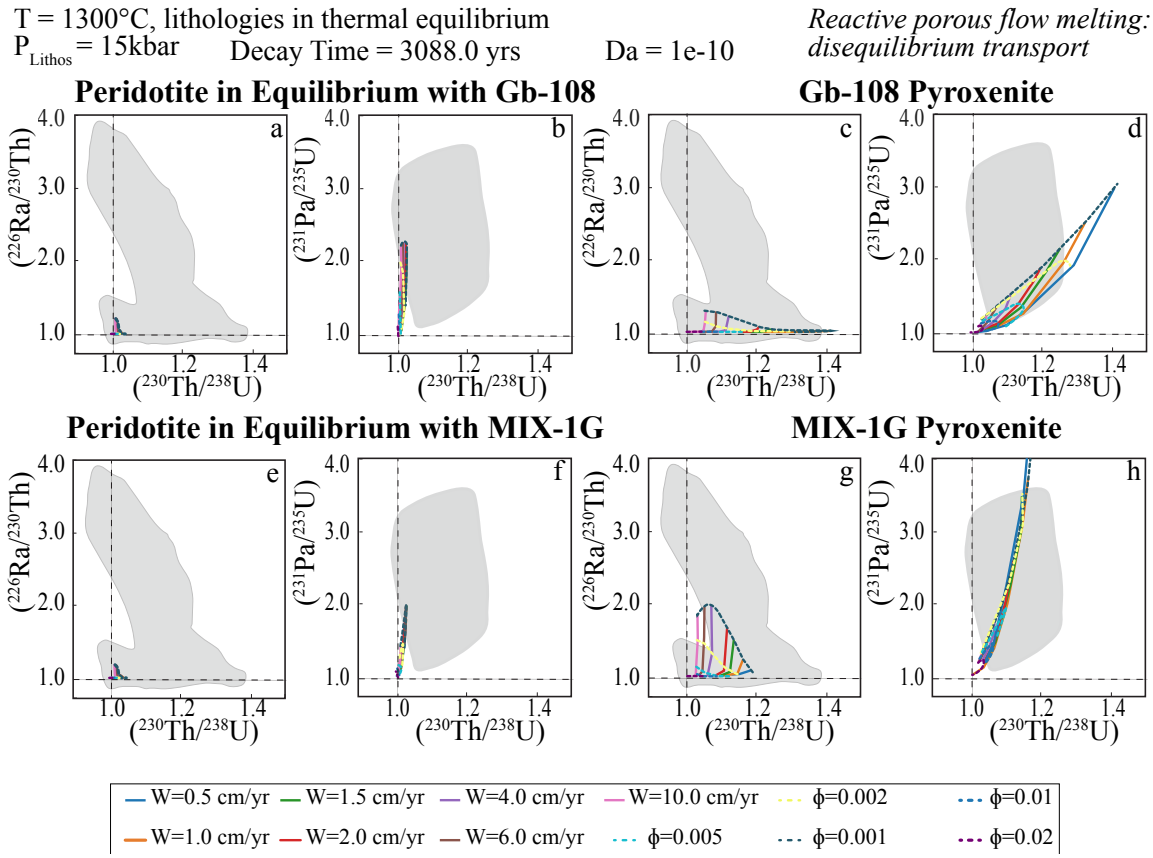

Figure 17. Gridded results for RPF disequilibrium transport melting calculations where T = 1300°C, the lithospheric cap (P_{Lithos}) is 10 kbar, the Damköhler number = 1 x 10^{-10}, a decay time of 3088.0 years, and peridotite and pyroxenite are in thermal equilibrium. The solid lines show partial melting outcomes with constant solid mantle upwelling rates (W), and the dashed lines show outcomes for constant maximum residual porosity values (ϕ). Panels and fields are as described in Figure 10.

4.1. RPF equilibrium and disequilibrium transport results: (^{230}Th/^{238}U)

From the RPF equilibrium and disequilibrium transport models tested here, I concluded that the (^{230}Th/^{238}U) ratios are near secular equilibrium for partial melts of peridotite in thermal equilibrium with Gb-108 and MIX1G (Figures 10-13). Calculated partial melting of Gb-108 generates (^{230}Th/^{238}U) activity ratios of 1.8 at 15 kbar (Figure 12c) and 1.6 at 10 kbar (Figure 10c). Corresponding partial melts of MIX1G pyroxenite have (^{230}Th/^{238}U) activity ratios of 1.3 at 15 kbar (Figure 12g) and 1.2 at 10 kbar (Figure 10g). These results demonstrate only minor differences in U-series disequilibria between

the two lithospheric thicknesses. Calculations for the pure radioactive decay of (^{230}Th/^{238}U) during lithospheric transport result in no notable differences after melting has stopped, as expected for the 75,000 yr half-life of ^{230}Th. The MIX1G partial melts and Gb-108 partial melts modeled here (Figure 10-17) thus have (^{230}Th/^{238}U) activity ratios greater than 1, regardless of lithospheric thickness, likewise expected for partial melts generated in the presence of residual garnet.

4.2 RPF equilibrium transport results: (^{226}Ra/^{230}Th) and (^{231}Pa/^{235}U)

Extremely high (^{226}Ra/^{230}Th) ratios were generated by the equilibrium transport model runs for Gb-108 and MIX1G pyroxenite partial melting (Figures 10, 12). The model results have corresponding peridotite partial melts with relatively high (^{226}Ra/^{230}Th) ratios (Figures 10, 12). These high (^{226}Ra/^{230}Th) ratios do not resemble the observed global MORB compositions.

While the (^{226}Ra/^{230}Th) for Gb-108 and MIX1G partial melts (Figures 11, 13) do decrease due to radioactive decay during lithospheric transport, the results are still not within the range of global MORB values for (^{226}Ra/^{230}Th). Partial melts of coexisting peridotite and the pyroxenite MIX1G, however, do overlap with the higher end of the global MORB range (Figures 11, 13). High (^{231}Pa/^{235}U) excesses are observed in all equilibrium transport model results and do not resemble global MORB data (Figures 10-13). Elkins et al. (2019) also observed high (^{231}Pa/^{235}U) excesses in a 5 kbar RPF equilibrium transport model run using identical inputs.

4.3 RPF disequilibrium transport results: ($^{226}Ra/^{230}Th$) and ($^{231}Pa/^{235}U$)

The results of disequilibrium transport model calculations at 10 kbar and 15 kbar for the peridotite in thermal equilibrium with Gb-108 (Figures 14, 16) and MIX1G (Figures 14, 16) have ($^{226}Ra/^{230}Th$) activity ratios under 1.6 and overall exhibit negligible differences between the two lithospheric thicknesses tested. After additional decay through the lithosphere, these ratios are further reduced to values under 1.2 (Figures 15, 17). Compared to global MORB data, these low results do not explain typical MORB compositions. Gb-108 partial melts (Figures 14, 16) have lower ($^{226}Ra/^{230}Th$) ratios than the outcomes of the equilibrium transport scenario, with much smaller differences between the 10 kbar and 15 kbar lithospheric caps. After further lithospheric transport and decay (Figures 15, 17), the ($^{226}Ra/^{230}Th$) ratios in Gb-108 partial melts are even lower and explain observed MORB data even less.

Calculated MIX1G partial melts, on the other hand, have ($^{226}Ra/^{230}Th$) ratios (Figures 14, 16) that align more closely with the observed MORB compositions, with only a slight discrepancy of ~0.2 at slower solid mantle upwelling rates (e.g., W = 0.5 cm/yr.). There are also negligible differences between the 10 kbar and 15 kbar outcomes (Figures 14, 16) prior to decay through the lithosphere. The results after radioactive decay during lithospheric transport for the same MIX1G model scenarios produce lower ($^{226}Ra/^{230}Th$) ratios that even more closely resemble the global MORB field (Figures 15, 17). ($^{226}Ra/^{230}Th$) ratios in MIX1G partial melts after decay during transport through the 10 kbar layer (Figure 15g) are higher by ~0.4 than at the 15 kbar layer (Figure 17g).

The calculated ($^{231}Pa/^{235}U$) results for the disequilibrium transport model are overall more comparable to typical MORB compositions than most of the ($^{226}Ra/^{230}Th$)

outcomes described above (Figures 14-17). Calculated ($^{231}Pa/^{235}U$) ratios for partial melts of peridotite in thermal equilibrium with Gb-108 and MIX1G (Figures 14-17) are essentially the same for melts at 10 kbar and 15 kbar depths. The ($^{231}Pa/^{235}U$) ratios for both the Gb-108 and the MIX1G pyroxenite melt products (Figures 15, 17) are notably lower than the results from the equilibrium transport models, with negligible differences between results for 10 kbar and 15 kbar depths. Comparisons of the ($^{226}Ra/^{230}Th$), ($^{230}Th/^{238}U$), and ($^{231}Pa/^{235}U$) ranges are listed in Table 2 below.

Table 2. Summary of modeling results for equilibrium and disequilibrium before and after lithospheric decay.

Mantle Component	Activity Ratio	Lithospheric Cap (kBar)	Equilibrium Transport Before Decay	Equilibrium Transport After Decay	Disequilibrium Transport Before Decay	Disequilibrium Transport After Decay
MIX-1G Pyroxenite	($^{226}Ra/^{230}Th$)	10	1.8 - 22.8	1.4 - 10.0	1.0 - 4.5	1.0 - 2.4
		15	1.9 - 20.4	1.2 - 6.1	1.0 - 4.7	1.0 - 2.0
	($^{231}Pa/^{235}U$)	10	1.8 - 17.4	1.7 - 16.7	1.0 - 5.1	1.0 - 5.0
		15	1.6 - 14.5	1.6 - 13.6	1.0 - 5.3	1.0 - 5.0
	($^{230}Th/^{238}U$)	10	1.1 - 1.3	1.1 - 1.3	1.0 - 1.2	1.0 - 1.2
		15	1.1 - 1.3	1.1 - 1.3	1.0 - 1.2	1.0 - 1.2
Peridotite in Equilibrium with MIX1G	($^{226}Ra/^{230}Th$)	10	1.1 - 4.5	1.1 - 2.4	1.0 - 1.4	1.0 - 1.2
		15	1.1 - 4.2	1.0 - 1.8	1.0 - 1.4	1.0 - 1.1
	($^{231}Pa/^{235}U$)	10	1.1 - 4.7	1.1 - 4.6	1.0 - 2.0	1.0 - 1.9
		15	1.1 - 4.5	1.1 - 4.3	1.0 - 1.9	1.0 - 1.9
	($^{230}Th/^{238}U$)	10	1.0 - 1.1	1.0 - 1.1	1.0 - 1.03	1.0 - 1.03
		15	1.0 - 1.1	1.0 - 1.1	1.0 - 1.03	1.0 - 1.03
Gb-108 Pyroxenite	($^{226}Ra/^{230}Th$)	10	0.99 - 4.2	0.99 - 2.3	1.0 - 1.9	1.0 - 1.4
		15	1.1 - 6.1	1.0 - 2.4	1.0 - 1.9	1.0 - 1.2
	($^{231}Pa/^{235}U$)	10	1.2 - 10.5	1.2 - 10.1	1.0 - 3.2	1.0 - 3.1
		15	1.3 - 10.3	1.3 - 9.7	1.0 - 3.1	1.0 - 3.0
	($^{230}Th/^{238}U$)	10	1.1 - 1.6	1.1 - 1.6	1.0 - 1.4	1.0 - 1.4
		15	1.1 - 1.8	1.1 - 1.7	1.0 - 1.4	1.0 - 1.4
Peridotite in Equilibrium with Gb-108	($^{226}Ra/^{230}Th$)	10	1.1 - 4.4	1.1 - 2.4	1.0 - 1.4	1.0 -1.2
		15	1.1 - 4.0	1.0 - 1.8	1.0 - 1.6	1.0 - 1.2
	($^{231}Pa/^{235}U$)	10	1.1 - 4.7	1.1 - 4.5	1.0 - 2.4	1.0 - 2.4
		15	1.1 - 4.3	1.1 - 4.1	1.0 - 2.3	1.0 - 2.2
	($^{230}Th/^{238}U$)	10	1.0 - 1.1	1.0 - 1.1	1.0 - 1.03	1.0 - 1.03
		15	1.0 - 1.1	1.0 - 1.1	1.0 - 1.03	1.0 - 1.03

5. Discussion

5.1 Lithologic transport effects on U-series disequilibria

5.1.1 Lithospheric Thickness Effects

A number of the model outcomes described above are noteworthy and require additional exploration. First, the RPF model outcomes are overall not significantly different between lithospheric depths at 10 kbar and 15 kbar. Secondly, most of the calculated U-series isotopes for partial melts from a single lithology fail to represent the global MORB data well, suggesting no single lithology can fully explain global oceanic basalt generation. These points are explored further below.

Seismic and geochemical evidence indicates a thicker axial lithosphere at detachment fault-bearing segments due to lower magmatic activity and a corresponding colder, thicker plate (Escartín et al., 2008; Klein & Langmuir, 1989). Detachment faults can remain active for tens of kilometers off-axis and are characterized by asymmetrical accretion with the axial lithospheric thickness up to 8 km thick (Escartín et al., 2008; Smith et al., 2012). In contrast, the oceanic lithosphere at faster-spreading ridges can have thicknesses ranging from 0 km at the spreading center to up to 100 km off-axis in the older oceanic crust (Naliboff et al., 2012). Per the discussion in previous sections, the greater lithospheric thicknesses might better represent more magma-starved segment with a long-lived detachment fault that shortens the top of the melting column at slow-spreading ridges like the KA Supersegment.

The 10 kbar (30 km) and 15 kbar (46 km) lithospheric caps used in this study provide a series of tests investigating how consequential the lithospheric thickness may be at slower-spreading ridge settings and directly contrast recent tests using similar

calculations for a thinner, 5 kbar lithosphere (Elkins et al., 2019). The peridotite partial melt RPF equilibrium transport modeling results of Elkins et al. (2019) are identical to the peridotite partial melts in my RPF equilibrium transport results. My RPF equilibrium and disequilibrium modeling results indicate a negligible change in most of the calculated U-series isotopes at 10 kbar and 15 kbar, suggesting the impact of deeper truncation of the melting regime on magma composition is typically minor. While the lithospheric thickness did not affect the generated results of this study, the lithospheric thickness may affect other oceanic settings such as ocean island settings and hotspot settings such as the Azores (e.g., Escartín et al., 2001; Prytulak & Elliott, 2009). Some outcomes of the RPF disequilibrium transport models that consider lithospheric decay may align better with global MORB data. In particular, ($^{226}Ra/^{230}Th$) ratios in MIX1G partial melts after decay through 10 kbar lithosphere (Figure 15g) are notably lower than melts after decay through 15 kbar (Figure 17g).

A few model outcomes did show some sensitivity to the final melting depth, however. For one, the calculated ($^{226}Ra/^{230}Th$) ratios in the partial melts of Gb-018 are higher in the 10 kbar and 15 kbar equilibrium RPF models than they were at 5 kbar (Elkins et al., 2019), indicating that thicker lithospheric caps may cause a higher ($^{226}Ra/^{230}Th$) ratio in partial melts of more silica-rich pyroxenites. Likewise, the RPF equilibrium transport model results of partial melts of Gb-108 at the 10 kbar and 15 kbar layers showed higher ($^{226}Ra/^{230}Th$) (4.2 versus 6.1, respectively) and higher ($^{230}Th/^{238}U$) (1.6 versus 1.8, respectively).

After transport and additional radioactive decay, however, ($^{226}Ra/^{230}Th$) in Gb-108 partial melts extracted from 10 kbar and 15 kbar depths were indistinguishable. This

result indicates a difference in residual minerals and bulk partitioning behavior for U, Th, and Ra between 5 kbar and 15 kbar, suggesting silica-excess pyroxenite rocks are more sensitive to the final melting depth than other lithologies.

The prediction of stable plagioclase in silica-rich eclogite under mantle conditions could be one possible explanation for the depth sensitivity of Gb-108 (Fabbrizio et al., 2009; Elkins et al., 2019). The presence of stable plagioclase might cause large ^{226}Ra deficits relative to ^{230}Th in RPF equilibrium transport of Gb-108 partial melts, resulting in high bulk Ra partition coefficients, where the deficits are atypical of the global MORB data (Elkins et al., 2019). Plagioclase in Gb-108 partial melts from calculated MELT-PX (Lambart et al., 2016) and pMELTS (Ghiorso et al., 2002) data show 18.6% plagioclase in the melt at 10 kbar and 6.3% at 15 kbar. The higher percent of plagioclase at 10 kbar may cause differences in the RPF equilibrium results of Gb-108. Further research can evaluate the impact of plagioclase and plagioclase solid/liquid partition coefficients on ^{226}Ra in pyroxenite partial melts. The decay time during transport through the lithosphere, however reduces the difference in ($^{226}Ra/^{230}Th$) for Gb-108 in RPF equilibrium transport, so it is less consequential in the final basalt, suggesting the ultimate impact of lithospheric depths is still relatively minor.

($^{231}Pa/^{235}U$) and ($^{230}Th/^{238}U$) ratios exhibit overall negligible differences between 10 kbar and 15 kbar scenarios, both before and after decay through the lithosphere. ($^{230}Th/^{238}U$) ratios are dependent on the depth of melting with pyroxenites melting in the garnet stability zone exhibiting higher ($^{230}Th/^{238}U$) ratios that do not necessarily change with varying lithospheric caps. Negligible changes in ($^{231}Pa/^{235}U$) indicate that it is not very sensitive to lithospheric thickness, perhaps because Pa is expected to be extremely

incompatible compared to U in all mantle minerals (including pyroxenitic minerals, to the limited extent those partition coefficients are known) (Figures 10-17, b, d, f, h). One explanation for the negligible difference in the (^{231}Pa/^{235}U) and (^{230}Th/^{238}U) ratios is the long half-life of ^{231}Pa and ^{230}Th. Since the half-lives of ^{231}Pa and ^{230}Th are 32,800 and 75,000 yrs., respectively (Figure 5; Bourdon et al., 2003), the decay times through the lithosphere of 2059 - 3088 yrs. have minimal effect on the calculated ratios, indicating these transport decay times may be negligible. The half-life alone may not account for the slight difference in (^{231}Pa/^{235}U) and (^{230}Th/^{238}U) ratios, however, partition coefficients may contribute more to differences in (^{231}Pa/^{235}U) ratios. The slight differences in the (^{231}Pa/^{235}U) and (^{230}Th/^{238}U) ratios might mean no significant mineralogical changes are affecting the bulk partition coefficients between these lithospheric thicknesses. The (^{230}Th/^{238}U) ratios for the peridotite partial melts are closer to secular equilibrium in the RPF equilibrium and disequilibrium transport models, which may be due to the more limited garnet stability range in ultramafic lithologies (i.e., garnet has a longer persistence time in the melting of pyroxenites due to its phase stability) (Hirschmann & Stolper, 1996; Lambart et al., 2016 and references therein).

5.1.2 Transport mechanism and mixing effects

Low age-constrained (^{231}Pa/^{235}U) and high (^{230}Th/^{238}U) ratios were measured in unaltered MORB samples from Jan Mayen Island, Kolbeinsey Ridge, Knipovich Ridge, and Mohns Ridge (a hotspot and three slow- to ultraslow spreading ridges) (Elkins et al., 2011, 2014, 2016b). These measured low (^{231}Pa/^{235}U) ratios from global MORB data are not reproduced by our (^{231}Pa/^{235}U) model results.

Lundstrom et al. (1998b) suggested that ($^{231}Pa/^{235}U$) ratios from the slow-spreading 33°S MAR had lower ($^{231}Pa/^{235}U$) in the actively upwelling segment, suggesting that ($^{231}Pa/^{235}U$) ratios are sensitive to the upwelling rate. Stracke et al. (2006) argued that channelized dynamic melting better explained variations in solid mantle upwelling rate (W) and porosity (ϕ) at MOR settings near Theistareykir, Iceland, suggesting that lower ϕ and higher W are needed to account for the large excess ^{226}Ra of melts with low ($^{230}Th/^{238}U$) ratios. Their modeling results and ^{231}Pa data indicated that porosity decreases towards the ridge axis (higher W). Using mineral-melt partition coefficients from Blundy and Wood (2003), Stracke et al. (2006) explore how U-series bulk partition coefficients affect dynamic model results.

For example, melting in the garnet-stability field has bulk partition coefficients that follow the order of $D_U > D_{Th} > D_{Pa} > D_{Ra}$ because of U-series incompatibility (Stracke et al., 2006). Due to the nearly perfect incompatibility of ^{231}Pa, the ^{231}Pa excess is suspected to rely on changes in D_U; these bulk partition coefficients can be changed by melting different mineralogical sources or pressure-dependent changes in mineral-melt partition coefficients (Stracke et al., 2006). My model accounted for changes in melting sources with different mineralogical sources and generated high ^{231}Pa and ^{226}Ra excess (Appendix A, Table S1). Partial melts of the pyroxenite compositions in my model outcomes do have high ($^{230}Th/^{238}U$) as well, due to the presence of stable garnet in the residual pyroxenite rock (Appendix A, Table S1, and references therein; Elkins et al., 2011, 2014, 2016b, 2019; Sims et al., 2002). These results fail to reproduce high ($^{230}Th/^{238}U$) ratios at the far end of the negative correlation with ($^{226}Ra/^{230}Th$) and the observed low ($^{231}Pa/^{235}U$) in some MORB (e.g., Jan Mayen Island; Elkins et al., 2016).

Based on my model results, I suggest that other melting scenarios (i.e., mixing of partial melts) may be more significant in certain ridge settings.

The individual lithologies tested here were unable to fully reproduce global MORB, particularly those with more enriched isotopic compositions and low age-constrained ($^{231}Pa/^{235}U$). Possible that mixtures of peridotite and pyroxenite partial melts may better explain the full range of global MORB data. Most of the ($^{226}Ra/^{230}Th$) and ($^{231}Pa/^{235}U$) pyroxenite model results for the RPF equilibrium transport were too high to explain the global MORB dataset. At the same time, most of my RPF disequilibrium ($^{226}Ra/^{230}Th$) and ($^{231}Pa/^{235}U$) pyroxenite and peridotite partial melt model results were too low to explain the global MORB dataset. Some MIX1G partial melts after extraction through the 10 kbar layer (Figure 15g), when mixed with the peridotite partial melts (Figure 15e) from RPF disequilibrium flow, more resemble the overall global MORB dataset. This observation suggests melting and mixing of melts from peridotite and silica-deficient pyroxenites in thermal equilibrium may explain some of the global MORB dataset.

Another possible scenario that could generate results closer to the global MORB data is a combination of Gb-108 and MIX1G pyroxenite partial melts and their partial peridotite melts in thermal equilibrium. Ultimately, it is highly unlikely that only one composition of pyroxenite and peridotite is melting in thermal equilibrium. It is more likely that a combination of pyroxenite and peridotite partial melt compositions is significantly more likely. Some combinations of the two pyroxenite partial melts can be explored in future research. Other studies have concluded that a combination of both pyroxenite and peridotite mantle sources might be needed to produce the observed

MORB signatures, and my outcomes broadly agree with those interpretations (e.g., Elkins et al., 2019; Lambart et al., 2013, 2016).

During lithospheric transport in the RPF equilibrium model, the ($^{226}Ra/^{230}Th$) ratios of Gb-108 partial melts mixed with coexisting peridotite partial melts (Figures 11, 13) might better explain more extreme MORB compositions, particularly for higher solid mantle upwelling rates and greater maximum residual porosities. This result would indicate that the partial melts would need higher solid mantle upwelling rates in a more porous melt column, perhaps in a high-porosity melt channel (e.g., Jull et al., 2002). As mentioned above, upwelling rates higher than 2.0 cm/yr may be extreme for the MOR settings of interest. In the future, samples from the Kane-Atlantis Supersegment could be compared to modeling results with some combination of MIX1G and Gb-108 pyroxenite and peridotite partial melts and lower upwelling ranges.

5.2 Implications of results from melting models

As observed above, my model outcomes revealed notable differences between traditional dynamic melting and new RPF disequilibrium transport partial melting calculations, although the two approaches aim to generate similar melt extraction mechanics.

Melt productivity (i.e., the rate at which a solid lithology melts during solid upwelling and decompression) is expected to be a significant contributing factor to melting outcomes, based on thermodynamically constrained MELT-PX predictions (Lambart et al., 2016) and the likely impact of changes in melt fraction on magma compositions (Asimow et al., 2001, 2004; Hirschmann & Stolper, 1996). Dynamic

melting results of Elkins et al. (2019) suggested low ($^{230}Th/^{238}U$) ratios modeled in basalts might be caused by a rapid increase in early melt production in a homogenous, peridotitic mantle where the melt was later diluted with instantaneous melts containing low ($^{230}Th/^{238}U$) ratios. This suggestion may indicate melt productivity variations in deeper melting (Elkins et al., 2019). Based on prior equilibrium RPF melting calculations, RPF models with melting at upwelling rates < 1 cm/yr, two porosity flow, and extraction via channelized flow may also be able to generate higher ($^{230}Th/^{238}U$); lower porosity RPF models with shallower melt extraction may generate lower ($^{230}Th/^{238}U$) ratios (Elkins et al., 2019; Sims et al., 2002).

Here I determined the outcomes for a RPF disequilibrium transport model at 5 kbar lithospheric thickness, with the same parameters described above, and directly compared disequilibrium RPF methods to dynamic melting calculations (Elkins et al., 2019). Below, Figure 18 shows the dynamic melting model results from Elkins et al. (2019), while Figure 19 shows my RPF disequilibrium transport model results for the same model input conditions.

For dynamic melting, Elkins et al. (2019) found a consistent, restricted range of outcomes for peridotites using the dynamic melting model, which was different from previous dynamic melting runs. For slower mantle upwelling rates, the partial peridotite melts for dynamic and disequilibrium RPF melting are notably similar, with just slightly higher ($^{226}Ra/^{230}Th$) and ($^{231}Pa/^{235}U$) in the dynamic melting scenario (Figure 18). The similarity between the modeled U-series isotopes in dynamic melting, and RPF disequilibrium indicates that new RPF disequilibrium transport has similar outcomes for

peridotite partial melts when compared to the dynamic melting calculation results of Elkins et al. (2019).

Prior studies suggest that the peridotite partial melting in a dynamic melting scenario is sufficient to explain U-series disequilibria observed in the global MORB dataset (e.g., Stracke et al., 2006). Per the discussion above, the consistent, restricted range of U-series outcomes for peridotite partial melts from RPF disequilibrium transport model support the dynamic melting results of Elkins et al. (2019) and suggests varying melt productivity during earlier melting, differing from Stracke et al. (2006).

Significant differences in calculated U-series disequilibria, specifically for partial melting of both MIX1G and Gb-108 pyroxenites, can be seen between the dynamic melting scenario at 5 kbar (Figure 18; Elkins et al., 2019) and the RPF disequilibrium transport model scenario (Figure 19), however. The dynamic melting results of Gb-108 and MIX1G partial melts (Figure 18) have higher ($^{226}Ra/^{230}Th$) and ($^{231}Pa/^{235}U$) consistently. The ($^{230}Th/^{238}U$) ratios for Gb-108 partial melts during dynamic melting are approximately equal in Figure 18c when compared to Figure 19c, while the ($^{230}Th/^{238}U$) ratios are lower in Figure 18d when compared with Figure 19d. For MIX1G partial melts, the ($^{230}Th/^{238}U$) ratios of the dynamic melting are higher (Figure 18). Discrepancies between Gb-108 partial melts from dynamic melting (Figure 18) and RPF disequilibrium transport (Figure 19) may indicate that silica-richness contributes to U-series disequilibria modeling results per the discussion above.

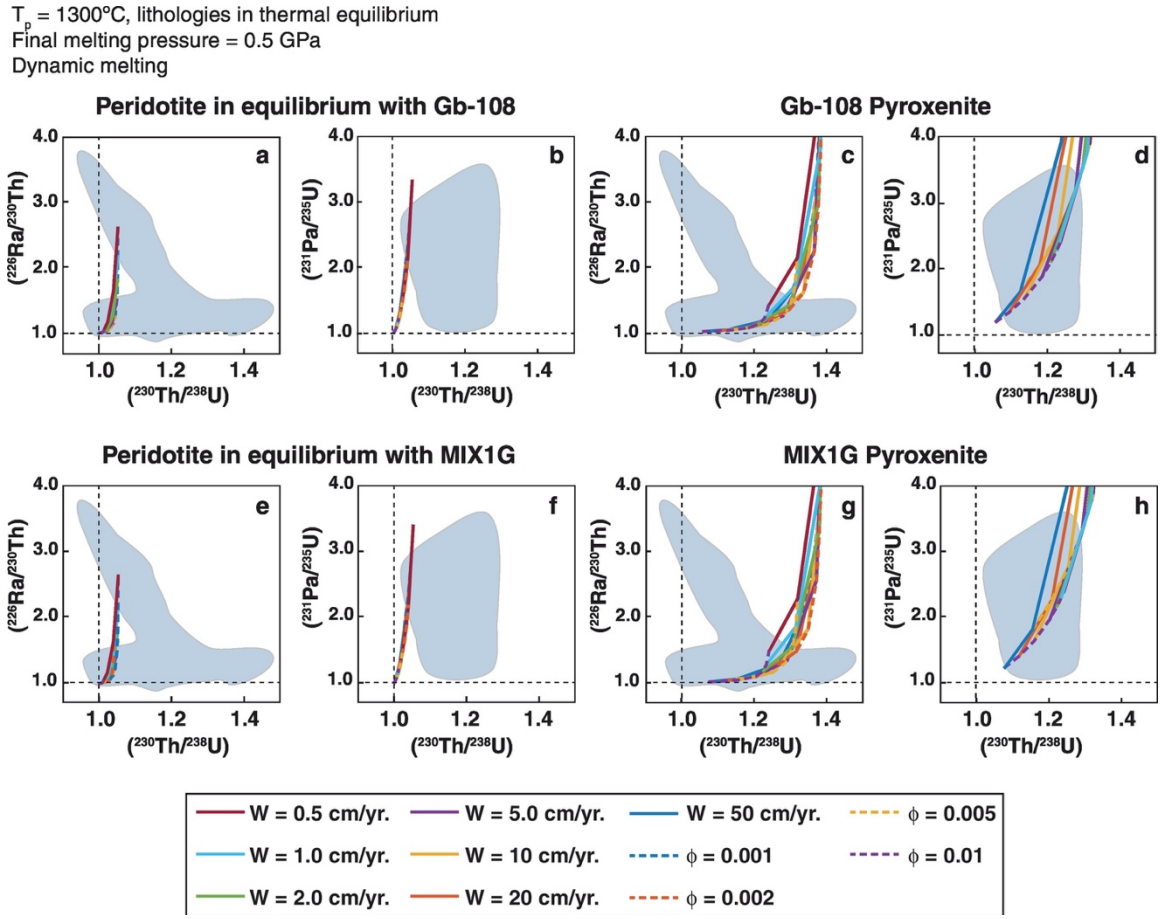

Figure 18. Gridded results for time-dependent dynamic melting calculations where T=1300°C, the lithospheric cap (P_{Lithos}) is 5 kbar, and peridotite and pyroxenite are in thermal equilibrium. The solid lines show model results for constant solid mantle upwelling rates (W), and the dashed lines show outcomes for constant maximum residual porosity values (ϕ). Global MORB data are shown as blue data fields. **a.** (^{226}Ra/^{230}Th) and **b.** (^{231}Pa/^{235}U) versus (^{230}Th/^{238}U) for partial melts of peridotite in thermal equilibrium with Gb-108 pyroxenite; **c.** (^{226}Ra/^{230}Th) and **d.** (^{231}Pa/^{235}U) versus (^{230}Th/^{238}U) for partial melts of Gb-108 pyroxenite; **e.** (^{226}Ra/^{230}Th) and **f.** (^{231}Pa/^{235}U) versus (^{230}Th/^{238}U) for partial melts of peridotite in equilibrium with MIX1G pyroxenite; and **g.** (^{226}Ra/^{230}Th) and **h.** (^{231}Pa/^{235}U) versus (^{230}Th/^{238}U) for partial melts of MIX1G pyroxenite, all after Elkins et al. (2019).

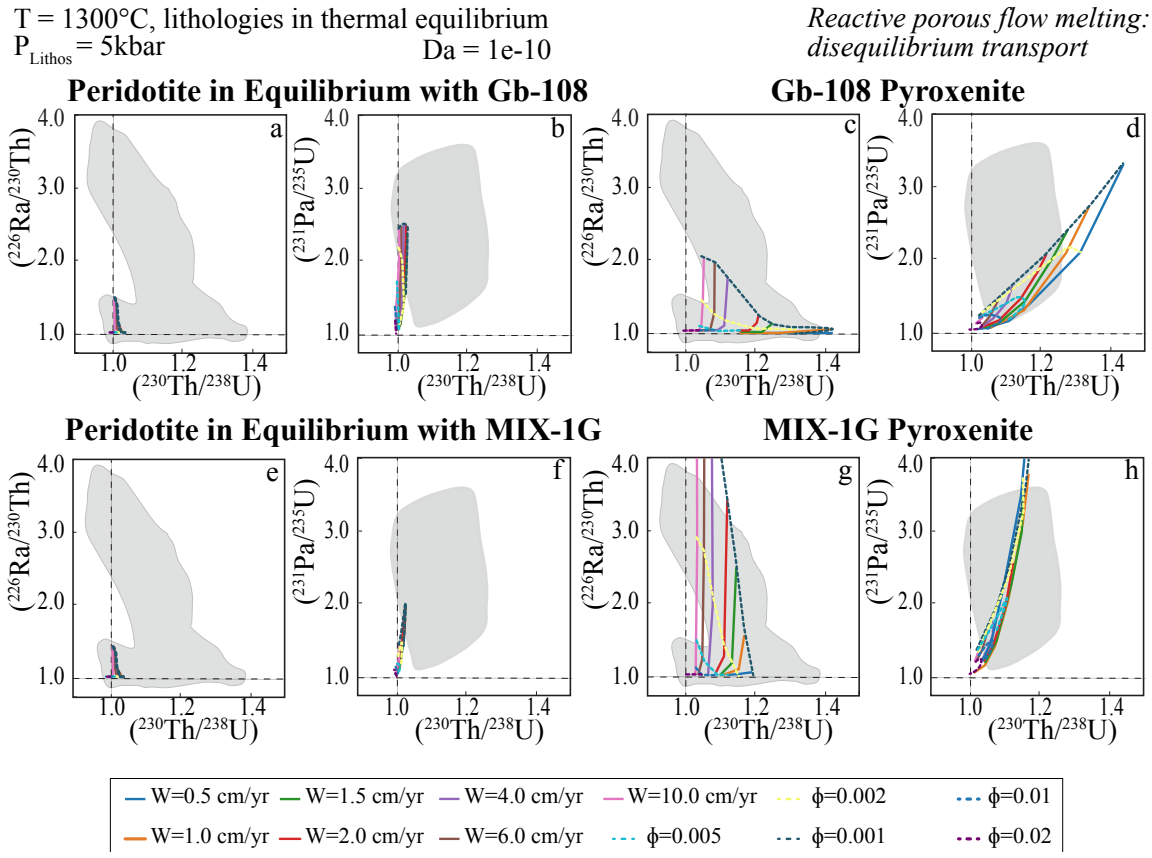

Figure 19. Gridded results for RPF disequilibrium transport melting calculations where T = 1300°C, the lithospheric cap (P_{Lithos}) is 5 kbar, the Damköhler number = 1 x 10^{-10}, and peridotite and pyroxenite are in thermal equilibrium. The solid lines show partial melting outcomes with constant solid mantle upwelling rates (W), and the dashed lines show outcomes for constant maximum residual porosity values (ϕ). Panels and fields are as described in Figure 10.

A closer look at the calculations are needed to better understand what may drive differences in model outcomes between dynamic melting and RPF disequilibrium transport. One of the significant differences between the two models is the manner of determining a critical porosity threshold for melt extraction and transport. Dynamic melting after McKenzie (1985) imposes a fixed critical porosity threshold – that is, the liquid in equilibrium with the solid is a fixed volume percentage of the source rock throughout the melting regime, neglecting compaction and two-phase flow effects. This setup results in outcomes where U-series isotopes are dominantly produced at the bottom

of the melt column and are then extracted instantaneously at the threshold, and where only fast transit will preserve shorter-lived isotopes like ^{226}Ra until eruption (Blundy & Wood, 2003; McKenzie, 1985; Prytulak & Elliott, 2009; Sims et al., 1999, 2002; Spiegelman & Elliott, 1993; Williams & Gill, 1989; Zou, 1998; Zou & Zindler, 2000). The partial melts under the critical threshold porosity are also held in local equilibrium, as in batch melting until the critical porosity threshold is met (Blundy & Wood, 2003; McKenzie, 1985; Zou, 1998).

Conversely, the RPF disequilibrium transport model is similar to a true accumulated fractional melting where the melt is extracted instantaneously, and the reference porosity imposes just the maximum liquid pore space at the top of the column (Spiegelman & Elliott, 1993). The rest of the melt zone has a more restricted porosity, whose mass fraction follows a simplified form of Darcy's Law; this local porosity and the permeability indirectly determine liquid flow rates in the RPF system, regardless of the degree of chemical equilibration between the two phases (solid and liquid) (Spiegelman & Elliott, 1993). The models allow for ingrowth of daughter nuclides through the entire melting column (Spiegelman & Elliott, 1993).

The differences in extraction rates and critical porosity thresholds on melting outcomes would also likely affect the shorter-lived isotopes of ^{226}Ra between the two models, particularly for lithologies that are more silica-rich or have faster solid upwelling rates. In particular, I observe overall higher ($^{226}Ra/^{230}Th$) ratios in the dynamic melting results (Figure 18) for pyroxenites. The higher ($^{226}Ra/^{230}Th$) ratios are likely due to the instantaneous transport calculation of ^{226}Ra, allowing it to be preserved from melting at the bottom of the melt column without calculating further aging, giving the maximum

disequilibria possible. Conversely, the RPF disequilibrium model outputs, particularly for Gb-108 partial melts (Figure 19c), have lower ($^{226}Ra/^{230}Th$) ratios that better explain some of the global MORB data set than the dynamic melting results of Gb-108 partial melts (Figure 18c).

Per the discussion above, the dynamic melting model is sensitive to solid mantle upwelling rates, melt extraction rates, and melt supply variations at the bottom of the melt column. RPF disequilibrium model results are sensitive to local porosity and permeability at both the top and bottom of the melt column. The differences of critical porosity (i.e., in dynamic melting) and local porosity at the top of the melting column (i.e., in RPF disequilibrium transport) may generate differences in the ($^{226}Ra/^{230}Th$), particularly for the pyroxenite partial melts. Considering the above comparison, RPF disequilibrium model results, compared with the dynamic melting results, may more closely represent extreme observed MORB data, particularly with some combination of peridotite and pyroxenite partial melts. I think the RPF disequilibrium model may be a suitable model to use in future analysis of U-series results from the Kane-Atlantis Supersegment to compare to the generated modeling results and determine if the model can explain the measurements. These results could then be compared major and trace elements from the segments to determine if melt supply and transport affects crustal accretion symmetry.

5.3 Ridge symmetry and supporting geochemical data

The above analysis employs a series of melting model tests and evaluates the sensitivity of partial melting outcomes to several important factors in the underlying melt regime. One goal of that analysis was to assess various melting model approaches as

tools for investigating the origins of seafloor morphology variations at slow-spreading rates, particularly for pyroxenite melting. In developing future approaches, basalt compositional characteristics like MgO, Na_2O, [Sr], and other major and trace elements are also affected by partial melting of mantle heterogeneities such as pyroxenite, and should be considered in conjunction with U-series isotope analysis to provide a more robust interpretation of melting relationships (Lissenberg & Dick, 2008; Klein & Langmuir, 1987; Murton & Rona, 2015; Humphris et al., 2015; Gale et al., 2013; Guo et al., 2021; Asimow et al., 2004; Elkins et al., 2011, 2016a; Lyu, 2019; Niu et al., 2001; Waters et al., 2011). Gale et al. (2013) looked at variations in major and trace element data of global mid-ocean ridge systems to provide a more robust statistical analysis for the global MORB dataset. Lyu (2019) more recently compared major and trace element data from asymmetrical and symmetrical ridges of the Kane Atlantis Supersegment in particular to evaluate the possible effects of mantle heterogeneity on melt composition that may, in turn, correlate with axial ridge symmetry. Except for MgO, Na_2O, [Sr], and Sr/Nd, Lyu (2019) found statistically insignificant differences in major and trace element compositions along symmetrical and asymmetrical segments for the Kane-Atlantis ridge. She found that basalt samples from asymmetrical, detachment-faulted ridge segments had higher mean MgO content, lower mean Na_2O content, and significantly lower [Sr] (Lyu, 2019).

The relative incompatibility of Sr and Nd during pure peridotite melting predicts relatively low Sr/Nd ratios should be observed in peridotitic partial melts (Salters & Stracke, 2004). Conversely, Sr is more compatible in pyroxenite melts, that should result in a higher basaltic Sr/Nd ratio (Stracke & Bourdon, 2009). For further comparison, Niu

et al. (2001) studied the Oceanographer-Hayes Ridge (33°N-35°N), a slow-spreading ridge north of the Kane Atlantis Supersegment. Niu et al. (2001) found that relative Sr enrichment in basalts correlates with topographic highs along the OH-3 ridge segment (e.g., a magma-starved segment), in agreement with the findings of Lyu (2019). Additional major and trace element analyses indicated that the size and fertility of passively-emplaced, enriched mantle heterogeneities melting beneath the ridge axis might influence the initiation and evolution of ridge segments (Niu et al., 2001). Guo et al. (2021) recently studied the same ridge segment using Sr-Nd-Hf isotopes and concluded that the inferred mantle heterogeneities comprise a combination of 1) ancient peridotite, 2) ancient metasomatic vein lithologies, and 3) refractory melts from the adjacent Azores mantle plume. Guo et al. (2001) suggested that those three mantle heterogeneities exert a dominant control on overlying ridge morphology and oceanic crustal thickness, perhaps similar to the nearby Kane-Atlantis ridge.

The combination of low MgO, higher Na_2O, [Sr], and Sr/Nd ratios may thus support the presence of pyroxenite and/or enriched peridotite sources melting beneath the symmetrical ridge segments (Lyu, 2019). These major and trace element systematics, in combination with higher ($^{230}Th/^{238}U$) and low ($^{226}Ra/^{230}Th$) and ($^{231}Pa/^{235}U$), might indicate melting in the presence of garnet and partial melting of heterogeneities like pyroxenites, based on my melting model outcomes and related recent results (Elkins et al., 2019). Higher pyroxenite concentrations in the melt zone should likewise produce enhanced magma supply to symmetrical ridge segments. In comparison, lower pyroxenite percentages in the source would result in comparatively magma starved, asymmetrical

ridge segments, agreeing with expectations for detachment fault formation and survival (Lambart et al., 2009; Lyu, 2019; Wilson et al., 2013).

6. Conclusion

As explored in this study, the compositions of partial melts from pyroxenite heterogeneities in the mantle can be predicted using a combination of dynamic melting and RPF equilibrium and disequilibrium transport models. Our RPF equilibrium and disequilibrium melting results support the requirement that a combination of mantle lithologies must be melting in much of the mantle to produce global MORB, but for U-series disequilibria, that process is relatively insensitive to oceanic lithospheric thickness.

Here I have calculated the U-series disequilibria in partial melts of a passively decompressing, bilithologic (peridotitic and pyroxenitic) upper mantle, using both equilibrium and disequilibrium transport RPF models with lithospheric caps of 10 kbar and 15 kbar. In detail, my results provide the following insights:

(1) Some studies suggest that oceanic lithospheric thickness may cause a noticeable difference in U-series disequilibria measurements (e.g., Elkins et al., 2019; Grose & Afonso, 2019). My study found no overall significant difference in U-series activity ratios between different oceanic lithospheric capping depths at 10 kbar and 15 kbar for RPF equilibrium and disequilibrium transport. The exceptions are ($^{226}Ra/^{230}Th$) in the partial melts of Gb-108 in the RPF equilibrium transport model and ($^{226}Ra/^{230}Th$) in the partial melts of MIX1G in the RPF disequilibrium transport model.

(2) High ($^{230}Th/^{238}U$) ratios were produced in the partial melts of MIX1G and Gb-108 pyroxenites due to melting in the presence of residual garnet throughout much of the

melting regime. Due to the more limited garnet stability range in ultramafic lithologies, the coexisting peridotite partial melts had comparatively low ($^{230}Th/^{238}U$) ratios.

(3) No calculated outcome of this study can fully explain the global MORB data set by melting a single, isolated lithology. Mixing melts from at least two lithologies, however, such as the combination of partial melts from MIX1G and Gb-108 pyroxenites and coexisting peridotites in thermal equilibrium, can better explain some of the global MORB data. This result is particularly noticeable for disequilibrium melt transport (fractional melt extraction) scenarios. Future U-series results of samples from the Kane-Atlantis Supersegment could be compared to these modeling results to determine if RPF disequilibrium transport and mixing of partial melts from heterogenous sources align with the measured samples.

(4) Dynamic melting and RPF disequilibrium transport models produce different results due to underlying assumptions about melt-solid equilibration (i.e., the presence of an equilibrated melt below a critical threshold porosity in dynamic melting) and permeability and compaction-driven differential magma transport rates. RPF disequilibrium melting model results may resemble global MORB data better than dynamic melting results of Elkins et al. (2019), particularly when some partial melts of peridotite and pyroxenite are combined.

(5) Regional MORB geochemistry and modeled U-series isotopes can be used together to better test for the presence of lithologic heterogeneities in the mantle of the Kane-Atlantis Supersegment. These tools can be used in the future to evaluate whether melting of more fusible and productive lithologies, like pyroxenite, may drive ridge axial faulting style at the KA Supersegment.

7. References

Abelson, M., and Agnon, A. (1997), Mechanics of oblique spreading and ridge segmentation. *Earth and Planet. Sci. Lett., 148(3-4)*, 405–421. doi: https://doi.org/10.1016/S0012-821X(97)00054-X.

Asimow, P.D., Hirschmann, M.M., and Stolper, E.M. (2001), Calculation of peridotite partial melting from thermodynamic models of minerals and melts, IV. Adiabatic decompression and the composition and mean properties of mid-ocean ridge basalts. *J. Petrology, 42(5)*, 963–998. doi: 10.1093/petrology/42.5.963.

Asimow, P.D., Dixon, J.E., and Langmuir, C.H. (2004), A hydrous melting model for mid-ocean ridge basalts: Application to the Mid-Atlantic Ridge near the Azores. *Geochem. Geophys. Geosyst., 5(1),* Q01E16. doi:10.1029/2003GC000568.

Blackman, D. K., Cann, J. R., Janssen, B., and Smith, D. K. (1998), Origin of extensional core complexes: Evidence from the Mid-Atlantic Ridge at Atlantis Fracture Zone. *J. Geophys. Res., 103(B9)*, 21315-21333, doi: https://doi.org/10.1029/98JB01756.

Blackman, D. K., Canales, P.J., and Harding, A. (2009), Geophysical signatures of oceanic core complexes, *Geophys. J. Int., 178(2),* 593-613. doi: 10.1111/j.1365-246X.2009.04184.x.

Blundy, J.D., Wood, B.J. (2003), Mineral-melt partitioning of uranium, thorium, and their daughters. *Rev. in Min., 59*–123.

Bourdon B., Henderson G. M., Lundstrom C. C., and Turner S. P. (2003), Uranium-series geochemistry. *Rev. Min. Geochem., 52*, 656.

Bourdon, B., Zindler, A., Elliott, T., and Langmuir, C.H. (1996), Constraints on mantle melting at mid-ocean ridges from global ^{238}U–^{230}Th disequilibrium data. *Nature,384*, 231–235. doi: 10.1038/384231a0.

Buck, W.R., Lavier, L.L., and Poliakov, A.N.B., 2005, Modes of faulting at mid-ocean ridges. *Nature, 434,* 719-723. doi: 10.1038/nature03358.

Cann, J. R., Blackman, D.K, Smith, D.K., McAllister, E., Janssen, B., Mello, S., Avgerinos, E., Pascoe, A.R., and Escartín, J. (1997), Corrugated slip surfaces formed at ridge–transform intersections on the Mid-Atlantic Ridge. *Nature, 385*, 329–332. doi: https://doi.org/10.1038/385329a0.

Colman, A., Sinton, J. M., White, S. M., McClinton, J. T., Bowles, J. A., Rubin, K. H., Behn, M. D., Cushman, B., Eason, D. E., Gregg, T. K. P., Gronvold, K., Hidalgo, S., Howell, J., Neill, O., Russo, R. (2012), Effects of variable magma supply on mid-ocean ridge eruptions: Constraints from mapped lava flow fields along the Galápagos Spreading Center. *Geochem. Geophys. Geosyst., 13(8),* Q08014. doi: 10.1029/2012GC004163.

Cooper, K.M., Goldstein, S.J., Sims, K.W.W., and Murrell, M.T. (2003), Uranium-series chronology of Gorda Ridge Volcanism: New evidence from the 1996 eruption. *Earth and Planet. Sci. Lett., 206(3-4),* 459-475. doi: 10.1016/S0012-821X(02)01083-X.

Dick H. J. B, Tivey M. A., Tucholke B. E. (2008), Plutonic foundation of a slow-spreading ridge segment: Oceanic core complex at Kane megamullion, 23°30′N, 45°20′W. *Geochem. Geophys. Geosyst., 9(5),* 1–44. doi: https://doi.org/10.1029/2007GC001645

Elkins, L.J., Bourdon, B., and Lambart, S. (2019), Testing pyroxenite versus peridotite sources for marine basalts using U-Series isotopes. *Lithos, 332-333,* 226-244. doi: https://doi.org/10.1016/j.lithos.2019.02.011.

Elkins L. J., Gaetani G. A. and Sims K. W. W. (2008), Partitioning of U and Th during garnet pyroxenite partial melting: constraints on the source of alkaline ocean island basalts. *Earth Planet. Sci. Lett., 265(1-2)*, 270–286. doi: https://doi.org/10.1016/j.epsl.2007.10.034.

Elkins, L.J., Scott, S.R., Sims, K.W.W., Rivers, E.R., Devey, C.W., Reagan, M.K., Hamelin, C., and Pedersen, R.B. (2016b). Exploring the role of mantle eclogite at midocean ridges and hotspots: U-series constraints on Jan Mayen Island and the Kolbeinsey Ridge: *Chemical Geology, 444,* 128–140. doi: 10.1016/j.chemgeo.2016.09.035.

Elkins, L.J., Sims, K.W.W., Prytulak, J., Elliott, T., Mattielli, N., Blichert-Toft, J., Blusztajn, J., Dunbar, N., Devey, C., Mertz, D.F., Schilling, J.G., and Murrell, M. (2011), Understanding melt generation beneath the slow-spreading Kolbeinsey Ridge using ^{238}U, ^{230}Th, and ^{231}Pa excesses. *Geochimica et Cosmochimica Acta, 75(21)*, 6300–6329. doi: 10.1016/j.gca.2011.08.020.

Escartín, J., Smith, D.K., Cann, J., Schouten, H., Langmuir, C.H., and Escrig, S. (2008), Central role of detachment faults in accretion of slow-spreading oceanic lithosphere: *Nature, 455*, 790–794. doi: 10.1038/nature07333.

Gale, A., Dalton, C.A., Langmuir, C.H., Su, Y., and Schilling, J.G. (2013), The mean composition of ocean ridge basalts: *Geochem. Geophys. Geosyst., 14(3)*, 489–518. doi: 10.1029/2012GC004334.

Ghiorso, M.S., Hirschmann, M.M., Reiners, P.W., and Kress III, V.C. (2002), The pMELTS: A revision of the MELTS for improved calculation of phase relations and major element partitioning related to partial melting of the mantle to 3GPa. *Geochem. Geophys. Geosyst., 3(5)*, 1-35. doi: 10.1029/2001GC000217.

Goldstein, S.J., Murrell, M.T., Jackecky, D.R. (1989), Th and U isotopic systematics of basalts from the Juan de Fuca and Gorda Ridges by mass spectrometry. *Earth and Planet. Sci. Lett*., *96(1-2)*, 134–146. doi: https://doi.org/10.1016/0012-821X(89)90128-3.

Goldstein, S.J., Murrell, M.T., Janecky, D.R., Delaney, J.R., Clague, D.A. (1992), Geochronology and petrogenesis of MORB from the Juan-De-Fuca and Gorda Ridges by ^{238}U-^{230Th} disequilibrium. *Earth and Planet. Sci. Lett.,109(1-2)*, 255–272. doi: https://doi.org/10.1016/0012-821X(92)90088-D.

Goldstein, S.J., Murrell, M.T., Williams, R.W. (1993), ^{231}Pa and ^{230Th} chronology of midocean ridge basalts. *Earth and Planet. Sci. Lett.,115(1-4),* 151–159. doi: https://doi.org/10.1016/0012-821X(93)90219-Y.

Grose, C.J. and Afonso, J.C. (2013), Comprehensive plate models for the thermal evolution of oceanic lithosphere. *Geochem. Geophys. Geosyst., 14(9),* 3751-3778. doi: 10.1002/ggge.20232.

Grose, C.J. and Afonso, J.C. (2019), Chemical disequilibria, lithospheric thickness, and the source of ocean island basalts. *J. Petrology, 60(4),* 755-790. doi: 10.1093/petrology/egz012.

Guo, P., Niu, Y., Sun, P., Zhang, J., Chen, S., Meng, D., Gong, H., and Wang, X. (2021),

The nature and origin of upper mantle heterogeneity beneath the Mid-Atlantic Ridge 33–35°N: A Sr-Nd-Hf isotopic perspective. *Geochimica et Cosmochimica Acta*, *307*, 72–85. doi: https://doi.org/10.1016/j.gca.2021.05.033.

Herzberg, C. (2004), Geodynamic information in peridotite petrology. *J. Petrology, 45(12),* 2507-2530. doi: 10.1093/petrology/egh039.

Hirschmann, M. M. and Stolper, E. M. (1996), A possible role for garnet pyroxenite in the origin of the "Garnet Signature" in MORB. *Contributions to Mineralogy and Petrology, 124,* 185-208. doi: https://doi.org/10.1007/s004100050184.

Hirschmann, M.M., Kogiso, T., Baker, M.B., and Stolper, E.M. (2003), Alkalic magmas generated by partial melting of garnet pyroxenite. *Geology, 31(6)*, 481–484. doi: https://doi.org/10.1130/0091-7613(2003)031<0481:AMGBPM>2.0.CO;2.

Hofmann, A.W. (1997), Mantle geochemistry: the message from oceanic volcanism. *Nature, 385*, 219–229.

Hofmann, A. (2003), Sampling Mantle Heterogeneity through oceanic basalts: Isotopes and trace elements. *Treatise on geochemistry*, *2*, 1-44. doi: 10.1016/B0-08-043751-6/02123-X.

Hole, M.J. and Millett, J.M. (2016), Controls of mantle potential temperature and lithospheric thickness on magmatism in the North Atlantic Igneous Province. *J. of Petrology, 57(2),* 417–436. doi: https://doi.org/10.1093/petrology/egw014.

Humphris, S.E., Tivey, M.K., and Tivey, M.A. (2015a), Deep-sea research II the Trans-Atlantic Geotraverse hydrothermal field : A hydrothermal system on an active detachment fault. *Deep-Sea Research Part II: Topical Studies in Oceanography, 121*, 8–16. doi: 10.1016/j.dsr2.2015.02.015.

Humphris, S.E., Tivey, M.K., and Tivey, M.A. (2015b), The Trans-Atlantic Geotraverse hydrothermal field: A hydrothermal system on an active detachment fault. *Deep-Sea Research Part II: Topical Studies in Oceanography, 121*, 8–16, doi: 10.1016/j.dsr2.2015.02.015.

Jull, M., Kelemen, P., and Sims, K. (2002), Consequences of diffuse and channelled porous melt migration on uranium series disequilibria. *Geochimica et Cosmochimica Acta, 66(23),* 4133–4148. doi: https://doi.org/10.1016/S0016-7037(02)00984-5.

Klein, E.M., and Langmuir, C.H. (1987), Global correlation of ocean ridge basalt chemistry with axial depth and crustal thickness. *J. of Geophys. Res., 92(B8)*, 8089-8115. doi: 10.1029/JB092iB08p08089.

Klein, E.M., and Langmuir, C.H. (1989), Local versus global in ocean ridge basalt Chemistry. *J. of Geophys. Res.*, *94(B4)*, 4241–4252. doi: https://doi.org/10.1029/JB094iB04p04241.

Klemme, S., Günther, D., Hametner, K., Prowatke, S., Zack, T. (2006), The partitioning of trace elements between ilmenite, ulvospinel, armalcolite and silicate melts with implications for the early differentiation of the moon. *Chemical Geology, 234(3-4),* 251–263. doi: https://doi.org/10.1016/j.chemgeo.2006.05.005.

Kogiso, T., Hirschmann, M.M., and Frost, D.J. (2003), High-pressure partial melting of garnet pyroxenite: possible mafic lithologies in the source of the ocean island basalts. *Earth and Planet. Lett., 216(4),* 603-617. doi: https://doi.org/10.1016/S0012-821X(03)00538-7.

Kogiso, T., Hirschmann, M.M., and Petermann, M. (2004), High-pressure partial melting

of mafic lithologies in the mantle. *J. Petrology, 45(12),* 2407-2422. doi: https://doi.org/10.1093/petrology/egh057.

de Koker, N.P., Lithgow-Bertelloni, C., and Stixrude, L. (2005), Dynamic topography and the density structure of the mantle lithosphere. *EOS, Trans. Am. Geophys. Un*., *86(52),* Fall Meet. Suppl., Abstract T23A-0524.

Kokfelt, T.F., Hoernle, K., Hauff, F. (2003), Upwelling and melting of the Iceland plume from radial variation of ^{238}U-^{230Th} disequilibria in postglacial volcanic rocks. *Earth and Planet. Sci. Lett., 214(1-2)*, 167–186. doi: https://doi.org/10.1016/S0012-821X(03)00306-6.

Lambart, S., Laporte, D., Schiano, P. (2013), Markers of the pyroxenite contribution in the major-element compositions of oceanic basalts: Review of the experimental constraints. *Lithos*, *160-161*, 14–36. doi: https://doi.org/10.1016/j.lithos.2012.11.018.

Lambart, S., Baker, M.B., and Stolper, E.M. (2016), The role of pyroxenite in basalt genesis: Melts-PX, a melting parameterization for mantle pyroxenites between 0.9 and 5 GPa. *J. Geophys. Res. Solid Earth, 121(8),* 5708-5735. doi: 10.1002/2015JB012762.

Lambart, S. (2017), No direct contribution of recycled crust in Icelandic basalts, *Geochem. Persp. Lett., 4,* 7-12, doi: 10.7185/geochemlet.1728.

Langmuir, C.H., Klein, E.M. and Plank, T. (1992), Petrological Systematics of Mid-Ocean Ridge Basalts: Constraints on Melt Generation Beneath Ocean Ridges. In *Mantle Flow and Melt Generation at Mid-Ocean Ridges* (eds J.P. Morgan, D.K. Blackman, and J.M. Sinton). doi: https://doi.org/10.1029/GM071p0183.

Lee, C.-T.A., and Chin, E. (2014), Calculating melting temperatures and pressures of peridotite protoliths: Implications for the origin of cratonic mantle. *Earth and Planet. Sci. Lett., 403*, 273–286. doi: https://doi.org/10.1016/j.epsl.2014.06.048.

Lissenberg, C.J., and Dick, H.J.B. (2008), Melt-rock reaction in the lower oceanic crust and its implications for the genesis of mid-ocean ridge basalt. *Earth and Planet. Sci. Lett., 271(1-4)*, 311–325, doi: 10.1016/j.epsl.2008.04.023.

Lundstrom, C.C., Gill, J., Williams, Q., Perfit, M.R. (1995), Mantle melting and basalt extraction by equilibrium porous flow. *Science, 270(5244)*, 1958–1961. doi: 10.1126/science.270.5244.1958.

Lundstrom, C.C., Gill, J., Williams, Q., Hanan, B.B. (1998a), Investigating solid mantle upwelling beneath mid-ocean ridges using U-series disequilibria. II. A local study at 33 degrees Mid-Atlantic Ridge. *Earth and Planet. Sci. Lett., 157*, 167–181.

Lundstrom, C.C., Williams, Q., Gill, J.B. (1998b), Investigating solid mantle upwelling rates beneath mid-ocean ridges using U-series disequilibria, 1: a global approach. *Earth and Planet. Sci. Lett., 157*, 151–165.

Lundstrom, C.C., Sampson, D.E., Perfit, M.R., Gill, J., Williams, Q. (1999), Insights into midocean ridge basalt petrogenesis: U-series disequilibria from the Siqueiros Transform, Lamont Seamounts, and East Pacific Rise. *J. Geophys. Res. Solid Earth, 104(B6)*, 13035–13048. doi: 10.1029/1999jb900081.

Lyu Y. (2019), Major and trace element analyses for studying oceanic crustal construction and ridge morphology along the Kane-Atlantis Supersegment of the Mid-Atlantic Ridge (Master's Thesis). Retrieved from DigitalCommons@UniversityOfNebraska-Lincoln.

(https://digitalcommons.unl.edu/geoscidiss/118/). Lincoln, NE: University of Nebraska-Lincoln.

Macdonald, K.C., Fox, P.J, Perram, L.J., Eisen, M.F., Haymon, R.M., Miller, S.P., Carbotte, S.M., Cormier, M.-H., and Shor, A.N. (1988), A new view of the mid-ocean ridge from the behaviour of the ridge-axis discontinuities. *Nature, 335,* 217-225. doi: https://doi.org/10.1038/335217a0.

MacLeod, C. J., Searle, R. C., Murton, B. J., Casey, J. F., Mallows, C., Unsworth, S. C., Achenbach, K. L., and Harris, M. (2009), Life cycle of oceanic core complexes. *Earth and Planet. Sci. Lett., 287(3-4)*, 333-344. doi: https://doi.org/10.1016/j.epsl.2009.08.016.

deMartin, B.J., Sohn, R.A., Canales, J.P., and Humphris, S.E. (2007), Kinematics and geometry of active detachment faulting beneath the Trans-Atlantic Geotraverse (TAG) hydrothermal field on the Mid-Atlantic Ridge. *The Geo. Soc. of America, 35(8),* 711-714. doi: 10.1130/G23718A.1.

McKenzie, D. (1985), ^{230}Th-^{238}U Disequilibrium and the Melting Processes Beneath Ridge axes. *Earth and Planet. Lett., 72(2-3),* 149-157, doi: 10.1016/0012-821X(85)90001-9.

McKenzie, D. and Bickle, M.J. (1988), The volume and composition of melt generated by extension of the lithosphere. *J. of Petrology, 29(3),* 625-679. doi: https://doi.org/10.1093/petrology/29.3.625.

McKenzie, D., Stracke, A., Blichert-Toft, J., Albarède, F., Grönvold, K., and O'Nions,

R.K. (2004), Source enrichment processes responsible for isotopic anomalies in oceanic island basalts. *Geochimica et Cosmochimica Acta*, *68(12)*, 2699–2724. doi: https://doi.org/10.1016/j.gca.2003.10.029.

Murton, B.J., and Rona, P.A. (2015), Carlsberg Ridge and Mid-Atlantic Ridge: Comparison of slow spreading centre analogues. *Deep-Sea Research Part II, 121*, 71–84. doi: 10.1016/j.dsr2.2015.04.021.

Naliboff, J.B., Lithgow-Bertelloni, C., Ruff, L.J., and de Koker, N. (2012), The effect of lithospheric thickness and density structure of Earth's stress field. *Geophys. J. Int., 1889(1),* 1-17. doi: 10.1111/j.1365-246X.2011.05248.x.

Navon, O. and Stolper, E. (1987), Geochemical consequences of melt percolation: The upper mantle as a chromatographic column. *J. Geol. 95*, 384–392. doi: https://doi.org/10.1086/629131.

Niu, Y., Bideau, D., Hékinian, R., Batiza, R. (2001), Mantle compositional control on the extent of mantle melting, crust production, gravity anomaly, ridge morphology, and ridge segmentation: a case study at the Mid-Atlantic Ridge 33-35°N. *Earth and Planet. Sci. Lett., 186(3-4)*, 383-399. doi: https://doi.org/10.1016/S0012-821X(01)00255-2.

Niu, Y., Langmuir, C.H., Kinzler, R.J. (1997), The origin of abyssal peridotites: A new perspective. *Earth and Planet. Sci. Lett., 152(1-4)*, 251-265. doi: https://doi.org/10.1016/S0012-821X(97)00119-2.

Olive, J.A., and Escartín, J. (2016), Dependence of seismic coupling on normal fault style along the Northern Mid-Atlantic Ridge. *Geochem. Geophys. Geosyst., 17(10)*, 1009-1020. doi: https://doi.org/10.1002/2016GC006460.

Peate, D.W., Hawkesworth, C.J., van Calsteren, P.W., Taylor, R.N.,Murton, B.J. (2001), ^{238}U-^{230Th} constraints on mantle upwelling and plume-ridge interaction along the Reykjanes Ridge. *Earth and Planet. Sci. Lett., 187(3-4)*, 259–272. doi: https://doi.org/10.1016/S0012-821X(01)00266-7.

Peirce, C. , Reveley, G., Robinson, A.H., Funnell, M.J., Searle, R.C., Simão, N.M., MacLeod, C.J., and Reston, T.J. (2019), Constraints on crustal structure of adjacent OCCs and segment boundaries at 13°N on the Mid-Atlantic Ridge. *Geophys. J. Int., 217(2),* 988-1010. doi: 10.1093/gji/ggz074.

Pertermann M. and Hirschmann M. (2003), Partial melting experiments on MORB-like pyroxenite between 2 and 3 GPa: constraints on the presence of pyroxenite in basalt source-regions from solidus location and melting rate. *J. Geophys. Res. 108(B2)*, 2125. doi:10.1029/2000JB000118.

Pertermann, M., Hirschmann, M.M., Hametner, K., Gunther, D., Schmidt, M.W. (2004), Experimental determination of trace element partitioning between garnet and silicarich liquid during anhydrous partial melting of MORB-like eclogite. *Geochem., Geophys., Geosyst., 5(5),* Q05A01. doi: https://doi.org/10.1029/2003GC000638.

Phipps Morgan J. (2001), Thermodynamics of pressure release melting of a veined plum pudding mantle. *Geochem. Geophys. Geosyst., 2(4).* doi: http://dx.doi.org/10.1029/2000GC000049.

Prytulak, J., and Elliott, T. (2009), Determining melt productivity of mantle sources from ^{238}U-^{230}Th and ^{235}U-^{231}Pa Disequilibria; an example from Pico Island, Azores. *Geochimica et Cosmochimica Acta, 73(7)*, 2103–2122. doi:

10.1016/j.gca.2009.01.001.

Reagan, M., Turner, S., Handley, H., Turner, M., Beier, C., Caulfield, J., Peate, D. (2017), ^{210}Pb-^{226}Ra disequilibria in young gas-laden magmas. *Sci. Reports, 7*, 45186. doi: 10.1038/srep45186.

Richter, F. M. (1986), Simple models for trace element fractionation during melt segregation. *Earth and Planet. Sci. Lett., 77(3-4)*, 333-344. doi: https://doi.org/10.1016/0012-821X(86)90144-5.

Rubin, K.H., van der Zander, I., Smith, M.C., Bergmanis, E.C. (2005), Minimum speed limit for ocean ridge magmatism from ^{210}Pb-^{226}Ra-^{230}Th disequilibria. *Nature, 437*, 534–538. doi: https://doi.org/10.1038/nature03993.

Rudge, J.F., Maclennan, J., and Stracke, A. (2013), The geochemical consequences of mixing melts from a heterogeneous mantle. *Geochimica et Cosmochimica Acta, 114,* 112–143. doi: 10.1016/j.gca.2013.03.042.

Russo, C. J., Rubin, K. H., Graham, D. W. (2009), Mantle melting and magma supply to the southeast indian ridge: The roles of lithology and melting conditions from U-series disequilibria. *Earth and Plant. Sci. Lett., 278 (1-2),* 55-66. doi: https://doi.org/10.1016/j.epsl.2008.11.016.

Salters, V.J., Dick, H.J. (2002), Mineralogy of the mid-ocean-ridge basalt source from neodymium isotopic composition of abyssal peridotites. *Nature, 418(6893)*, 68–72. doi: 10.1038/nature00798.

Salters, V.J.M., and Longhi, J. (1999), Trace element partitioning during the initial stages of melting beneath mid-ocean ridges. *Earth and Planet. Sci. Lett., 166(1-2),* 15–30. doi: https://doi.org/10.1016/S0012-821X(98)00271-4.

Salters, V.J.M. and Stracke, A. (2004), Composition of the depleted mantle. *Geochem. Geophys. Geosyst., 5(5),* Q05B07. doi:10.1029/2003GC000597.

Scott, D.R., and Stevenson, J. (1989), A self-consistent model of melting, magma migration and buoyancy-driven circulation beneath Mid-Ocean Ridges. *J. Geophys. Res.*, *94*, 2973–2988. doi: https://doi.org/10.1029/JB094iB03p02973.

Sloan, H., and Patriat, P. (2004), Reconstruction of the flanks of the Mid-Atlantic Ridge, 28° to 29° N: Implications for evolution of young oceanic lithosphere at slow-spreading centers. *Geochem. Geophys. Geosyst., 5(9),* Q09006. doi:10.1029/2004GC000727.

Sims, K.W.W., DePaolo, D.J., Murrell, M.T., Baldridge, W.S., Goldstein, S., Clague, D., Jull, M. (1999), Porosity of the melting zone and variations in the solid mantle upwelling rate beneath Hawaii: Inferences from ^{238}U-^{230}Th-^{226}Ra and ^{235}U-^{231}Pa disequilibria. *Geochimica et Cosmochimica Acta, 63(23-24)*, 4119–4138. doi: https://doi.org/10.1016/S0016-7037(99)00313-0.

Sims, K.W.W., Goldstein, S.J., Blichert-Toft, J., Perfit, M.R., Kelemen, P., Fornari, D.J., Michael, P., Murrell, M.T., Hart, S.R., DePaolo, D.J., Layne, G., Ball, L., Jull, M., Bender, J. (2002), Chemical and isotopic constraints on the generation and transport of magma beneath the East Pacific Rise. *Geochimica et Cosmochimica Acta, 66(19),* 3481–3504. doi: https://doi.org/10.1016/S0016-7037(02)00909-2.

Smith, D.K. and Cann, J.R. (1993), Building the crust at the Mid-Atlantic Ridge. *Nature, 365*, 704-717. doi: https://doi.org/10.1038/365707a0.

Smith, D.K., Cann, J.R., and Escartín, J. (2006), Widespread active detachment faulting

and core complex formation near 13°N on the Mid-Atlantic Ridge. *Nature, 442*, 440–443. doi: 10.1038/nature04950.

Smith, D.K.,Escartín, J., Schouten, H., Cann, J.R. (2012), Active long-lived faults emerging along slow-spreading mid-ocean ridges. *Oceanography, 25(1)*, 94–99. doi: http://dx.doi.org/10.5670/oceanog.2012.07.

Spiegelman, M. and Elliott, T. (1993), Consequences of melt transport for uranium series disequilibrium in young lavas. *Earth and Planet, Sci. Lett., 118(1-4),* 1-20. doi: https://doi.org/10.1016/0012-821X(93)90155-3.

Spiegelman, M. (2000), UserCalc: A web based uranium series calculator for magma migration problems. *Geochem. Geophys. Geosyst., 1(8),* 1-8. doi: https://doi.org/10.1029/1999GC000030.

Standish, J.J., and Sims, W.K.K (2010), Young off-axis volcanism along the ultraslow-spreading Southwest Indian Ridge. *Nature Geosciences, 3*, 286-292. doi: http://www.nature.com/doifinder/10.1038/ngeo824.

Stracke, A., Zindler, A., Salters, V. J.M., McKenzie, D., and Grönvold, K. (2003), The dynamics of melting beneath Theistareykir, northern Iceland. *Geochem. Geophys. Geosyst., 4(10),* 8513, doi:10.1029/2002GC000347.

Stracke, A., Bourdon, B., McKenzie, D. (2006), Melt extraction in the Earth's mantle: constraints from U-Th-Pa-Ra studies in oceanic basalts. *Earth and Planet. Sci. Lett., 244(1-2)*, 97–112. doi: https://doi.org/10.1016/j.epsl.2006.01.057.

Tepley, F.J., Lundstrom, C.C., Sims, K.W.W., Hekinian, R. (2004), U-series disequilibria

in MORB from the Garrett Transform and implications for mantle melting. *Earth and Planet. Sci. Lett., 223(1-2)*, 79–97. doi: https://doi.org/10.1016/j.epsl.2004.04.010.

Tucholke, B. E., Lin, J., and Kleinrock, M. C. (1998), Megamullions and mullion structure defining oceanic metamorphic core complexes on the Mid-Atlantic Ridge. *J. Geophys. Res., 103(B5)*, 9857–9866. doi: https://doi.org/10.1029/98JB00167.

Tucholke, B. E., Fujioka, K., Ishihara, T., Hirth, G., and Kinoshita, M. (2001), Submersible study of an oceanic megamullion in the central North Atlantic. *J. Geophys. Res.*, *106(B8),* 16145– 16161. doi:10.1029/2001JB000373.

Turner, S., Kokfelt, T., Hauff, F., Haase, K., Lundstrom, C., Hoernle, K., Yeo, I.A., Devey, C. (2015), Mid-ocean ridge basalt generation along the slow-spreading, South Mid-Atlantic Ridge (5-11°S): Inferences from ^{238}U-^{230}Th-^{226}Ra disequilibria. *Geochimica et Cosmochimica Acta, 169*, 152–166. doi: https://doi.org/10.1016/j.gca.2015.07.036.

Turner, S., Kokfelt, T., Hoernle, K., Lundstrom, C., Hauff, F., 2016, 231Pa systematics in postglacial volcanic rocks from Iceland. *Geochimica et Cosmochimica Acta, 185,* 129–140. doi: https://doi.org/10.1016/j.gca.2015.12.011.

Waters, C.L., Sims, K.W.W., Perfit, M.R., Blichert-Toft, J., and Blusztajn, J. (2011), Perspective on the genesis of E-MORB from chemical and isotopic heterogeneity at 9-10°n East Pacific Rise. *J. of Petrology*, *52(3)*, 565–602. doi: 10.1093/petrology/egq091.

Waters, C.L., Sims, K.W.W., Klein, E.M., White, S.M., Reagan, M.K., Girard, G. (2013),

Sill to surface: Linking young off-axis volcanism with subsurface melt at the overlapping spreading center at 9°03'N East Pacific Rise. *Earth and Planet. Sci. Lett., 369-370*, 59–70. doi: https://doi.org/10.1016/j.epsl.2013.03.006.

Williams, R.W. and Gill, J.B. (1989), Effects of partial melting on uranium decay series. *Geochimica et Cosmochimica Acta, 53(7)*, 1607–1619. doi: https://doi.org/10.1016/0016-7037(89)90242-1.

Wilson, S.C., Murton, B.J., and Taylor, R.N. (2013), Mantle composition controls the development of an Oceanic Core Complex. *Geochem., Geophys., Geosyst., 14(4)*, 979–995. doi: 10.1002/ggge.20046.

White, W.M., and Klein, E.M. (2014), *Composition of the Oceanic Crust*: Elsevier Ltd., *4*, 457–496. doi: 10.1016/B978-0-08-095975-7.00315-6.

White, W., and Schilling, J.-G. (1978), The nature and origin of geochemical variation in Mid-Atlantic Ridge basalts from the Central North Atlantic. *Geochimica et Cosmochimica Acta, 42(10)*, 1501–1516. doi: 10.1016/0016-7037(78)90021-2.

Yaxley, G.M., Sobolev, A.V. (2007), High-pressure partial melting of gabbro and its role in Hawaiian magma source. *Contrib. Mineral Petrol., 154,* 371-383. doi: https://doi.org/10.1007/s00410-007-0198-4.

Zhiteng, Y., Jiabiao, L., Yuyang, L., Xiqiu, H., Jie, Z., and Lei, Z. (2013), Distribution of large-scale detachment faults on mid-ocean ridges in relation to spreading rates. *Acta Oceanol. Sin., 32(12),* 109-117. doi: 10.1007/s13131-013-0397-y.

Zou, H.B. (1998), Trace element fractionation during modal and nonmodal dynamic

melting and open-system melting: A mathematical treatment. *Geochimica et Cosmochimica Acta, 62(11)*, 1937-1945. doi: https://doi.org/10.1016/S0016-7037(98)00115-X.

Zou, H.B. (2007), *Qualitative Geochemistry*. London: Imperial College Press.

Zou, H.B. and Zindler, A. (2000), Theoretical studies of ^{238}U-^{230}Th-^{226}Ra- and ^{235}U-^{231}Pa disequilibria in young lavas produced by mantle melting. *Geochimica et Cosmochimica Acta, 64(10)*, 1809-1817. doi: https://doi.org/10.1016/S0016-7037(00)00350-1.

Appendix A

Table S1. Fixed mineral/melt partition coefficients used to calculate bulk rock partition coefficients in model calculations for this study after Elkins et al. (2019).

Lithology	Phase	D_U	D_{Th}	D_{Pa}[a]	D_{Ra}[a]	Sources
Garnet peridotite	Garnet	0.038	0.017	0.00001	0.00001	RD 1097-5 experiment, Salters et al. (2002)
	Clinopyroxene	0.003	0.004	0.00001	0.00001	RD 1097-5 experiment, Salters et al. (2002)
	Olivine	0.00005	0.00047	0.00001	0.00001	RD 1097-5 experiment, Salters et al. (2002)
	Orthopyroxene	0.0078	0.0086	0.00001	0.00001	TM0500-3 experiment, Salters et al. (2002)
	Spinel	0.012	0.0024	0.00001	0.00001	Lunar basalt, Klemme et al. (2006)
Spinel peridotite	Clinopyroxene	0.008	0.007	0.00001	0.00001	TM 1094-9 experiment, Salters & Longhi (1999)
	Olivine	0.00005	0.00047	0.00001	0.00001	RD 1097-5 experiment, Salters et al. (2002)
	Orthopyroxene	0.0024	0.0027	0.00001	0.00001	RD 1097-2 experiment, Salters et al. (2002)
	Plagioclase	0.0006	0.0034	0.00001	0.02000	D_U,D_{Th} calculated after Blundy & Wood (2003), D_{Ra} from Fabbrizio et al. (2009)
	Spinel	0.012	0.0024	0.00001	0.00001	Lunar basalt, Klemme et al. (2006)
Gb-108 pyroxenite	Garnet	0.02405	0.0041	0.00001	0.00001	A343 experiment, Pertermann et al. (2004)
	Clinopyroxene	0.0041	0.0032	0.00001	0.00001	Pertermann et al. (2004)

	Olivine	0.00005	0.00047	0.00001	0.00001	RD 1097-5 experiment, Salters et al. (2002)
	Plagioclase	0.0006	0.0034	0.00001	0.02000	D_U,D_{Th} calculated after Blundy & Wood (2003), D_{Ra} from Fabbrizio et al. (2009)
	Spinel	0.046	0.016	0.00001	0.00001	Maximum measured, Elkins et al. (2008)
MIX1G pyroxenite	Garnet	0.013	0.0032	0.00001	0.00001	Experimental results, Elkins et al. (2008)
	Clinopyroxene	0.017	0.015	0.00001	0.00001	Experimental results, Elkins et al. (2008)
	Olivine	0.00005	0.00047	0.00001	0.00001	RD 1097-5 experiment, Salters et al. (2002
	Spinel	0.046	0.016	0.00001	0.00001	Maximum measured, Elkins et al. (2008)
	Orthopyroxene	0.0078	0.0086	0.00001	0.00001	TM0500-3 experiment, Salters et al. (2002)
	Plagioclase	0.0006	0.0034	0.00001	0.02000	D_U,D_{Th} calculated after Blundy & Wood (2003), D_{Ra} from Fabbrizio et al. (2009)

[a] By convention, D_{Pa} and D_{Ra} are set to $1x10^{-5}$ for most minerals, except D_{Ra} in plagioclase.